

A Radiation Algorithm with Correlated- k Distribution. Part I: Local Thermal Equilibrium

J. LI

Canadian Center for Climate Modeling and Analysis, Meteorological Service of Canada, Victoria, British Columbia, Canada

H. W. BARKER

Cloud Physics Research Division, Meteorological Service of Canada, Downsview, Ontario, Canada

(Manuscript received 5 April 2004, in final form 5 August 2004)

ABSTRACT

A new radiation scheme is proposed that uses the correlated- k distribution (CKD) method. The definition of the k -distribution function, the transformation between frequency space and k space, and the upper limit of the absorption coefficient in cumulative probability space (CPS) are discussed. The corresponding relation between each interval in CPS and the heating rate profile provides a method for determining the width of intervals in CPS. Three schemes are discussed for handling the spectral overlap of gases. Method 1 rearranges the appropriate combination of gaseous absorption coefficients when the spectral overlap of two gases is extensive. Method 2 applies to most overlapping gases and addresses the most important aspects of each gas's spectrum in each interval of CPS. Method 3 applies to weak gases only and seeks to adjust the main absorption coefficients in order that radiative forcing at the surface and the top of the atmosphere is correct. This model is quite efficient because 1) relatively few intervals in CPS are used (up to 1 mb, only 35 intervals for solar radiation, and 46 for infrared); 2) for some intervals with very large absorption coefficients, the radiative transfer process is simplified by ignoring scattering; 3) the water vapor continuum is dealt with efficiently by neglecting its effect in some nonimportant intervals in CPS and at high altitudes; and 4) gaseous overlap methods are simple and effective. Moreover, this model contains a proper treatment of spectral overlap between solar and infrared radiation. For both solar and infrared radiation, heating rate errors are generally less than 0.2 K day^{-1} , and errors in flux at the surface and the top of the atmosphere are generally less than 1 W m^{-2} .

1. Introduction

Over the past decade, there has been a trend in radiative transfer schemes to replace traditional band models for gaseous transmittance with the correlated- k distribution (CKD) method (Goody et al. 1989; West et al. 1990; Lacis and Oinas 1991; Fu and Liou 1992; Holling 1993; Kratz 1995; Edwards and Slingo 1996; Mlawer et al. 1997; Chou and Suarez 1999; Sun and Rikus 1999; Kato et al. 1999; Yang et al. 2000; Chou et al. 2001; Zhang et al. 2003). The advantages of the CKD over the band model are obvious. Sorting absorption coefficients in ascending order transforms the problem of integrating a tortuously variable absorption coefficient over frequency space into integrating a smooth sorted absorption coefficient using relatively few quasi-

monochronic quadrature points. In principle, CKD can be applied to a single absorption line while band models address only the mean values for bands. Another well-known characteristic of the CKD method is that it readily incorporates the scattering of photons by clouds, aerosols, and molecules.

In this study we introduce an accurate and efficient CKD model that is suitable for use by the climate modeling community. First, the definition of the k -distribution function and the transformation between frequency space and k space will be discussed briefly. Also how to determine the referenced absorption coefficients in the cumulative probability space (CPS) will be addressed.

The approach used to handle gaseous overlap is a key issue for any CKD radiative transfer model. In the present paper, three methods are discussed for gaseous overlap. Method 1 emphasizes the rearrangement of combined spectra for two gases. It is suitable for cases where the interaction of two gases is very strong. Method 2 is the method applied in most situations. It is based on the finding that the rearrangement of the ab-

Corresponding author address: Dr. Jiangnan Li, Canadian Center for Climate Modeling and Analysis, Meteorological Service of Canada, P.O. Box 1700, University of Victoria, Victoria, BC V8P 2Y2, Canada.
E-mail: Jiangnan.Li@ec.gc.ca

sorption coefficient for each gas in only a portion of CPS can capture the main characteristics of the k distribution. Method 3 is used for minor gases by simply fitting results to make the forcings correct.

The efficiency of CKD model has not been considered too seriously by past developers of CKD models. It is shown here that different intervals in CPS play different heating rate roles as a function of altitude. This characteristic of the CKD can be harvested to dramatically simplify the calculation process. Also, model efficiency is improved by simple treatments of the overlap between the water vapor continuum and other gases.

2. Gaseous transmission

a. Correlated- k distribution

Assuming a uniform source of radiation over the frequency interval $\Delta\nu$, gaseous transmittance is

$$\text{Tr}(w) = \frac{1}{\Delta\nu} \int_{\Delta\nu} e^{-w k(\nu)} d\nu, \quad (1)$$

where w is the absorber amount, and $k(\nu)$ is the gaseous absorption coefficient in frequency space. In actuality, $k(\nu)$ also depends on temperature T and pressure p . The transmission function can also be written in k space (Goody and Yung 1989) as

$$\text{Tr}(w) = \int_0^\infty e^{-w k} f(k) dk, \quad (2)$$

where $f(k)$ is the k -distribution function, with

$$f(k) = \frac{1}{\Delta\nu} \int_{\Delta\nu} \delta[k - k(\nu)] d\nu, \quad (3)$$

where $\delta[k - k(\nu)]$ is the δ function and $f(k)$ is the Dirac comb (see appendix A), for it sums up all absorption lines of the same strength. In (2) and (3), k is still the absorption coefficient, but it is now in k space and thus represents reordered values that are independent of ν . Note that k space and frequency space could transform each other as

$$\begin{aligned} \text{Tr}(w) &= \int_0^\infty e^{-w k} f(k) dk, \\ &= \int_0^\infty e^{-w k} \frac{1}{\Delta\nu} \int_{\Delta\nu} \delta[k - k(\nu)] d\nu dk, \\ &= \frac{1}{\Delta\nu} \int_{\Delta\nu} \int_0^\infty e^{-w k} \delta[k - k(\nu)] dk d\nu, \\ &= \frac{1}{\Delta\nu} \int_{\Delta\nu} e^{-w k(\nu)} d\nu. \end{aligned} \quad (4)$$

Now consider the cumulative probability function

$$g(k) = \int_0^k f(k') dk', \quad (5)$$

with $g(0) = 0$ and $g(\infty) = 1$. From (5), $dg(k) = f(k)dk$, which when inserted into (2) yields

$$\text{Tr}(w) = \int_0^1 e^{-w k(g)} dg. \quad (6)$$

As such, g forms a CPS, in which $k(g)$ is now the absorption coefficient in CPS. Scaling CPS into N points G_i ($i = 0, 1, 2, \dots, N$), with $G_0 = 0$, $G_N = 1$, and letting $g_i = G_i - G_{i-1}$, with $\sum_{i=1}^N g_i = 1$, the integral in (6) becomes

$$\text{Tr}(w) = \sum_{i=1}^N \int_{G_{i-1}}^{G_i} e^{-w k(g)} dg. \quad (7)$$

Accurate results for each of the N intervals in (7) must be obtained through line-by-line calculations. On the other hand, the transmission function in a k -distribution model has to be calculated as

$$\text{Tr}(w) = \sum_{i=1}^N e^{-w \langle k(g_i) \rangle} g_i. \quad (8)$$

For each domain g_i , the model absorption coefficient in CPS, $\langle k(g_i) \rangle$, could be obtained through fitting to the line-by-line results of (7) in the same domain for a suitable range of w . In appendix B, a proof is given for the inequality relation:

$$\int_{G_{i-1}}^{G_i} e^{-w k(g)} dg \geq \exp \left[-w \frac{1}{g_i} \int_{G_{i-1}}^{G_i} k(g) dg \right] g_i,$$

which implies that

$$\langle k(g_i) \rangle = \frac{\alpha_i}{g_i} \int_{G_{i-1}}^{G_i} k(g) dg, \quad (9)$$

where $\alpha_i \leq 1$, and the equality holding for constant $k(g)$ within the interval $G_{i-1} \leq g \leq G_i$.

As mentioned above, in order for the transmission function to match line-by-line results, $\langle k(g_i) \rangle$ has to be obtained by some fitting procedure. This represents the lion's share of the work when building a CKD model. Equation (9), however, provides an important upper limit for $\langle k(g_i) \rangle$. Since the results of the fitting process depend on the range chosen for w , (9) can be a criterion for the correctness of the fit. When the integral interval g_i is very narrow (usually for intervals very close to 1 in CPS), $k(g)$ can be considered to be approximately constant. This leads directly to $\langle k(g_i) \rangle$ since α_i is very close to 1. Also, it is generally found that $\alpha_i = 1$ approximately holds for the water vapor continuum since variations in absorption coefficients are then much smaller than for water vapor lines.

For an inhomogeneous atmosphere, the transmission

function between any two levels depends on the gaseous amount and absorption coefficients along a path between the two levels. For the transmission function between two pressures p_1 and p_2 ,

$$\text{Tr} = \sum_{i=1}^N \exp \left[- \int_{p_1}^{p_2} \langle k(g_i) \rangle q(p) \frac{dp}{G} \right] g_i, \quad (10)$$

where $q(p)$ is the mass mixing ratio for the absorber at pressure p , and G is the gravitational constant. This is known generally as the correlated- k distribution method. “Correlated” refers to the correlation in CPS between the sorted gaseous absorption coefficients at different p . In general, however, this kind of correlation is not completely satisfied within a range of typical atmospheric conditions. Specifically, a satisfactory sorting of $k(g)$ at one pressure level may be decidedly unsatisfactory at another level. However, if the two model pressure levels are not too far apart, the correlation in sorting could be largely kept in the atmospheric condition (West et al. 1990; Fu and Liou 1992).

As mentioned above, $\langle k(g_i) \rangle$ is actually $\langle k(g_i, p, T) \rangle$. In the model, $\langle k(g_i, p, T) \rangle$ is calculated for a number of reference pressures and is fitted as a polynomial in temperature as

$$\langle k(g_i, p_r, T) \rangle = \sum_{n=0}^4 c_i(g_i, p_r)(T - 250)^n, \quad (11)$$

where p_r are reference pressure levels. A total of 28 pressure levels are distributed between 1000 and 0.005 mb, 10 of which are above 1 mb. In section 4 it is shown that for some g_i , calculations need be done only for the surface to 1 mb. For these cases, only 18 values of p_r are needed. Thus, $\langle k(g_i, p, T) \rangle$ at any arbitrary pressure can be obtained by linear interpolation between two neighboring p_r . The fit in (11) is valid between 160 and 340 K, which includes most atmospheric conditions.

Figure 1 shows solar and infrared radiative heating rates corresponding to different g_i for the midlatitude summer profile (MLS) (McClatchey et al. 1972), with H_2O in 4200–8400 and 0–340 cm^{-1} . It can be seen that different g_i correspond to heating rates in different vertical regions. This is a general and very important characteristic of the CKD method. A brief discussion is necessary to reveal the related physics. Usually the variation of absorption coefficients in CPS is huge, often spanning 10 or more orders of magnitude. Thus, for a g_i located very close to 1 in CPS, the corresponding absorption coefficients must be very large. Therefore, incoming solar radiation attributed to such a g_i is attenuated quickly in the upper atmosphere and so produces large localized heating rates. The farther away g_i are from 1 in CPS, the smaller their corresponding absorption coefficients and attenuation. This enables solar photons to penetrate the atmosphere, producing localized heating at progressively lower levels.

Similarly, in the infrared, a g_i located very close to 1 in CPS with large absorption coefficients contributes mostly to cooling the very high atmosphere. Meanwhile, in the lower atmosphere, where absorber densities are relatively large, optical depths will be large too, and gaseous transmission will be close to zero. Hence, the local emission will be absorbed locally, so cooling rates are very small because almost no energy is lost. Conversely, at high altitudes where absorber densities become low and optical depths become much smaller than in the lower atmosphere, local emission can escape, thereby cooling the surroundings. On the other hand, for smaller absorption coefficients, optical depth in the high atmosphere becomes small and emission is weak. As such, little energy is lost and cooling proceeds slowly. Therefore, for a g_i with a certain magnitude of absorption coefficients, emission and transmission will play important roles at a unique and rather localized altitude, thereby affecting a local cooling rate.

Since maximum heating rates for each g_i appear at different heights, total heating rates show oscillatory forms with small amplitudes (see the rhs of Fig. 1). Therefore, errors in heating rate relative to line-by-line calculations should also appear as oscillatory forms. By restricting the amplitude of the oscillatory heating rate errors, the interval width for each g_i can be determined. This is the criterion used to determine the distribution of g_i in CPS. Table 1 lists all considered gases and their spectral intervals in this model.

b. Overlap of two or more gases

1) METHOD 1 (DIRECT COMBINED GAS MAPPING)

Method 1 is only applied to cases in which the overlap of two gases is strong, such as H_2O and CO_2 in the 540–800- cm^{-1} band. The optical depths for H_2O and CO_2 are $\tau_{\text{H}_2\text{O}}(\nu) = \int_{\Delta p} k_{\text{H}_2\text{O}}(\nu, p, T) q_{\text{H}_2\text{O}}(dp'/G)$ and $\tau_{\text{CO}_2}(\nu) = \int_{\Delta p} k_{\text{CO}_2}(\nu, p, T) q_{\text{CO}_2}(dp'/G)$, where $k_{\text{H}_2\text{O}}(\nu, p, T)$ and $k_{\text{CO}_2}(\nu, p, T)$ are absorption coefficients for H_2O and CO_2 , respectively, and $q_{\text{H}_2\text{O}}$ and q_{CO_2} are mass mixing ratios for H_2O and CO_2 , respectively. Here, Δp is the vertical integral interval in pressure. Total optical depth for the two gases is

$$\tau_{\text{CO}_2}(\nu) + \tau_{\text{H}_2\text{O}}(\nu) = \int_{\Delta p} k(\nu, p, T) q_{\text{CO}_2} dp'/G,$$

where $k(\nu, p, T) = k_{\text{CO}_2}(\nu, p, T) + r k_{\text{H}_2\text{O}}(\nu, p, T)$, and $r = q_{\text{H}_2\text{O}}/q_{\text{CO}_2}$. The $k_{\text{CO}_2}(\nu, p, T) + r k_{\text{H}_2\text{O}}(\nu, p, T)$ is rearranged to represent the absorption coefficient of a “single” gas. However, since r varies with atmospheric profile and location, sorting cannot generally be done. Since the variation of r can be very large in the lower atmosphere, five reference values for $r = 0.06, 0.24, 1, 4, 16$ are defined below 1 mb, and only one reference value of $r = 0.06$ above 1 mb. For each reference r , the

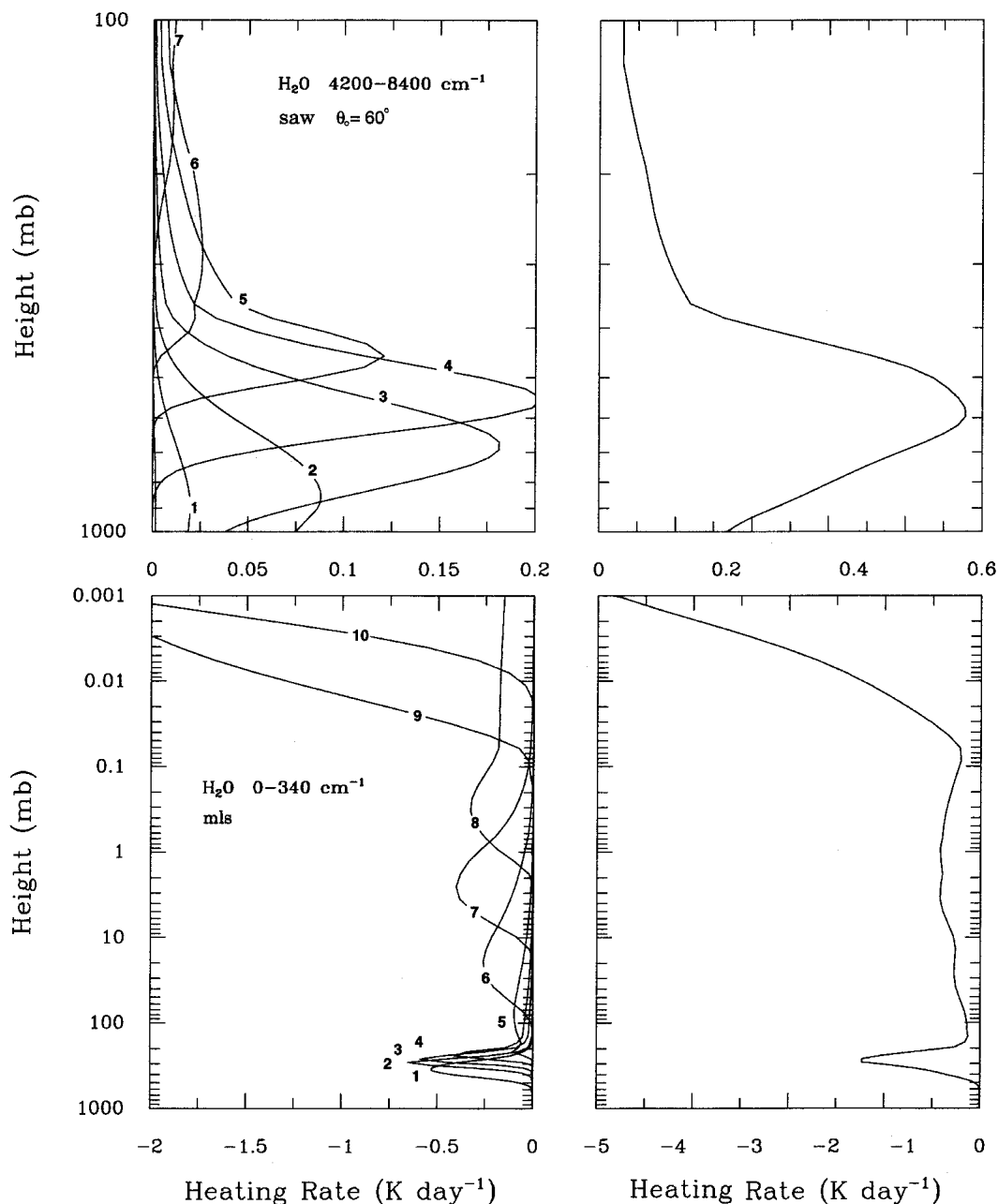


FIG. 1. (left) Heating rate profiles for the MLS atmosphere corresponding to different intervals in CPS for H_2O in (top) 4200–8400 and (bottom) 0–340 cm^{-1} . The number on each curve is the interval number. (right) The sum of heating rates for all intervals.

temperature dependence expansion for a given reference pressure is given by (11). Method 1 has been discussed in a similar way by others (West et al. 1990; Lacis and Oinas 1991; Fu and Liou 1992; Mlawer et al. 1997). What is emphasized here is the proper interpolation of r ; otherwise, the results are not valid for a wide range of applications.

Figure 2 shows the spectral sorting results in 540–800 cm^{-1} . As for $r = 0.05$, $k_{\text{CO}_2}(g, p, T)$ is sorted nicely in

ascending order in CPS, but $k_{\text{H}_2\text{O}}(g, p, T)$ is a considerable mess since sorting was based largely on the CO_2 spectrum. The dashed line in the top panel shows that the total result for sorting $k_{\text{CO}_2}(g, p, T) + rk_{\text{H}_2\text{O}}(g, p, T)$ is very close to sorting just CO_2 . Generally, $r = 0.05$ occurs at altitudes above 100 mb where CO_2 dominates the heating rate and the nicely sorted spectrum for CO_2 could produce accurate results for CO_2 . For H_2O , the spectrum is sorted poorly and so it is difficult to pro-

TABLE 1. The band spectrum ranges, absorber, and the number of intervals in CPS. The intervals in CPS are divided into three categories: major, minor, and minor only applied to the region above 1 mb. The number of intervals for continuum shown in parentheses indicates how many intervals in each band of CPS continuum the calculation is done.

	Band (cm^{-1})	Absorber		No. of intervals in CPS				Solar weight (W m^{-2})
				Major	Minor	Minor (above 1 mb)	Continuum	
Solar	14 500–50 000	$\text{O}_3, \text{O}_2, \text{H}_2\text{O}$	0.2–0.69 μm	6	3			628.5946
	8400–14 500	$\text{H}_2\text{O}, \text{O}_3, \text{O}_2$	0.69–1.19 μm	4	3	1		438.2265
	4200–8400	$\text{H}_2\text{O}, \text{CO}_2$	1.19–2.381 μm	6	3	1		246.9080
	2500–4200	$\text{H}_2\text{O}, \text{CO}_2$	2.381–4 μm	4	6	3		40.5737
				Total	20	15		1354.3028 W m^{-2}
	2200–2500	$\text{H}_2\text{O}, \text{CO}_2, \text{N}_2\text{O}$	4.0–4.545 μm	1	1	3	0	3.6754
	1900–2200	$\text{H}_2\text{O}, \text{N}_2\text{O}$	4.535–5.263 μm	1	1		(2)	2.7949
	1400–1900	H_2O	5.263–7.143 μm	2	2	1	(3)	3.2008
	1100–1400	$\text{H}_2\text{O}, \text{N}_2\text{O}, \text{CH}_4, \text{CFC11}, \text{CFC12}, \text{CFC113}, \text{CFC114}$	7.143–9.05 μm	3	4		(3)	1.1388
								+6.47=1360.7731
Infrared	980–1100	$\text{H}_2\text{O}, \text{O}_3, \text{CO}_2, \text{CFC11}, \text{CFC12}, \text{CFC113}, \text{CFC114}$		2	3	1	(4)	0.3184
	800–980	$\text{H}_2\text{O}, \text{CO}_2, \text{CFC11}, \text{CFC12}, \text{CFC113}, \text{CFC114}$		2	0		(1)	0.3537
	540–800	$\text{H}_2\text{O}, \text{CO}_2, \text{N}_2\text{O}, \text{O}_3$		3	6	1	(3)	0.2956
	340–540	H_2O		6	2	1	(4)	0.099 62
	0–340	H_2O		4	3	3	(4)	0.023 22
				Total	24	22	10	+5.3405=1366.1136 W m^{-2}

duce accurate results. However, in the high atmosphere with $r = 0.05$, the role of H_2O is much weaker than that of CO_2 .

As for $r = 1$, it is shown that in comparison with the results of $r = 0.05$, $k_{\text{H}_2\text{O}}(g, p, T)$ becomes better sorted, but the absorption lines are still an unstructured shape. At the same time, $k_{\text{CO}_2}(g, p, T)$ becomes slightly less regularly sorted.

For $r = 15$, $k_{\text{H}_2\text{O}}(g, p, T)$ becomes slightly more regular, but $k_{\text{CO}_2}(g, p, T)$ still shows a well-sorted pattern with many lines matching the sorted curve $k_{\text{CO}_2}(g, p, T) + rk_{\text{H}_2\text{O}}(g, p, T)$. This is because the variation of $k_{\text{CO}_2}(g, p, T)$ is much larger than that of $k_{\text{H}_2\text{O}}(g, p, T)$. Even for $r = 100$, $k_{\text{CO}_2}(g, p, T)$ is still more regularly sorted than that of $k_{\text{H}_2\text{O}}(g, p, T)$.

Figure 3 shows cooling rates and model errors (model minus line by line) for H_2O only, CO_2 only, $\text{H}_2\text{O} + \text{CO}_2$, and $\text{H}_2\text{O} + \text{CO}_2 + \text{N}_2\text{O} + \text{O}_3$. Line-by-line calculations shown in this paper are based on the 1996 High-Resolution Transmission (HITRAN 96) with spectral line shape wing-cut 25 cm^{-1} . Three atmospheric profiles are considered: MLS, tropical (TRO), and subarctic winter (SAW). Results for upward flux at the top of atmosphere (TOA) and downward flux at the surface are shown in Table 2. In the first column of Fig. 3, errors in the cooling rate for H_2O are up to 0.5 K day^{-1} with flux errors reaching as much as 10 W m^{-2} . Figure 2 shows that, in general, the spectrum of H_2O is not sorted well compared to that for CO_2 . Therefore, cooling rate and flux are simulated poorly for the case of H_2O alone. Generally, for a poorly sorted pattern of gaseous absorption coefficients in CPS, gaseous transmission cannot be handled accurately by CKD using just a few intervals in CPS be-

cause the information is scrambled and so the attractive feature of the CKD method shown in section 2a is lost. Compared to H_2O , the results for CO_2 alone are much better, with errors in cooling rate less than 0.04 K day^{-1} below 100 mb and flux less than 2 W m^{-2} . Errors in cooling rate become larger in the higher regions since the CO_2 cooling rate becomes larger in the high atmosphere; the relative errors are unchanged.

For the region above 0.01 mb, errors increase to over 1 K day^{-1} . This is because there are too few intervals in the region very close to 1 in CPS. There are only 10 intervals in CPS for $540\text{--}800 \text{ cm}^{-1}$, and only 2 of them are major contributors to the cooling rate above 0.01 mb. Errors in this region could easily be reduced by increasing the number of g_i located very close to 1. This is not done, however, since CO_2 cooling rates could be dramatically influenced by the nonlocal thermal equilibrium (LTE) effect. For now, there is little motivation to achieve accurate results above 0.01 mb.

Figure 3c depicts results for $\text{H}_2\text{O} + \text{CO}_2$. It shows that errors in cooling rate and flux (Table 2) are largely reduced compared to the case of H_2O only. Also, errors are slightly reduced compared to CO_2 only because sorting was based on the results of $\text{H}_2\text{O} + \text{CO}_2$.

In $540\text{--}800 \text{ cm}^{-1}$, H_2O and CO_2 interactions are very strong especially in the lower atmosphere. Here, strong interaction means that both gases play important roles in the same region. Therefore, the two gases have to be handled together, especially in the lower atmosphere. Generally, transmission for the sum of two gaseous absorption coefficients is not equal to the multiple of two transmissions for each of the two gases. For gases 1 and 2,

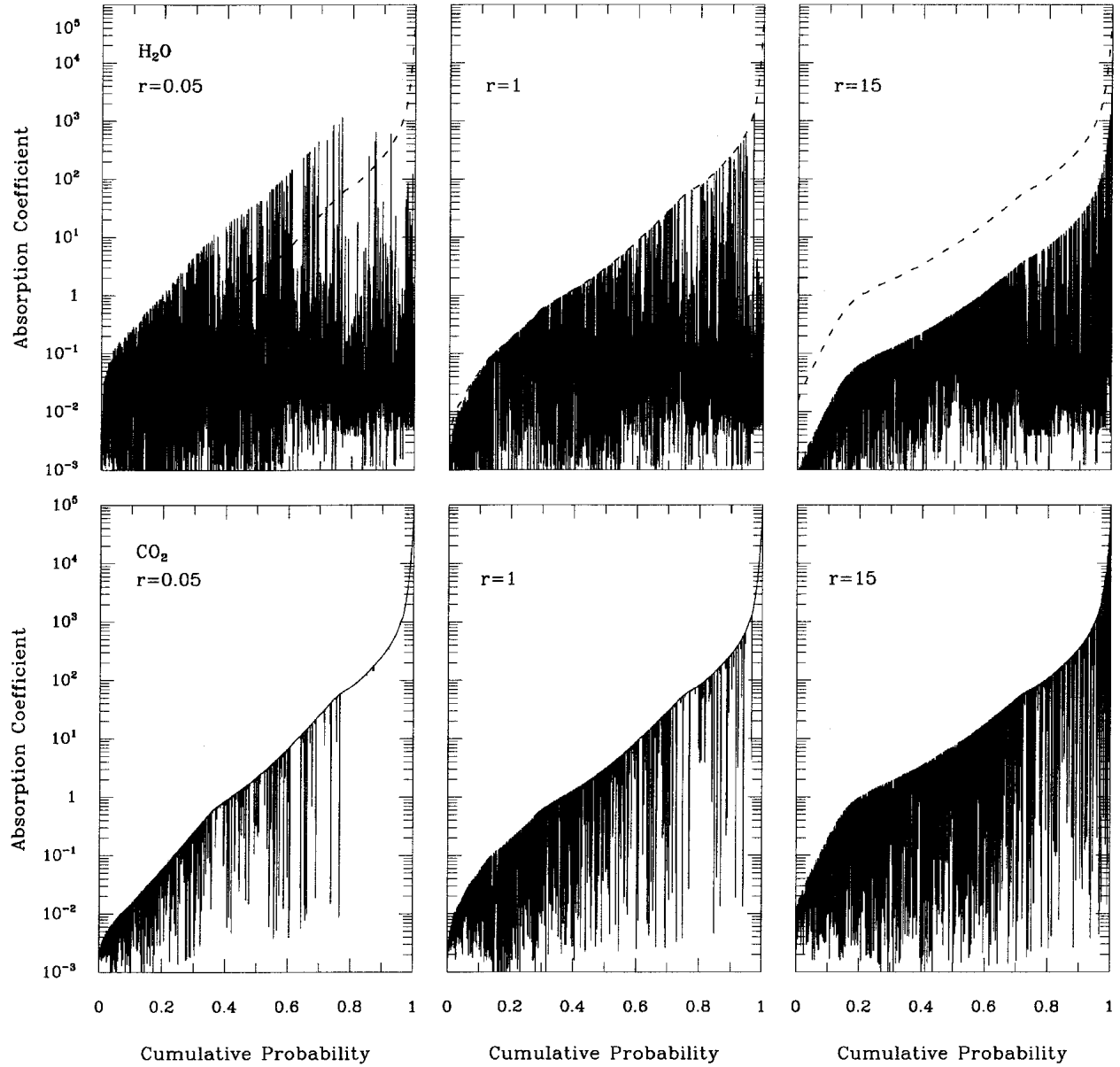


FIG. 2. Various rearrangements of absorption coefficients in CPS for 540–800 cm^{-1} based on sorting $k_{\text{CO}_2}(\nu, p, T) + rk_{\text{H}_2\text{O}}(\nu, p, T)$ with $r = 0.05$, $r = 1$, and $r = 15$. (top) $k_{\text{H}_2\text{O}}(\nu, p, T)$, and (bottom) $k_{\text{CO}_2}(\nu, p, T)$. (top) The dashed lines are for $k_{\text{CO}_2}(\nu, p, T) + rk_{\text{H}_2\text{O}}(\nu, p, T)$. The pressure is 200 mb and the temperature is 250 K.

$$\begin{aligned}
 \text{Tr}_{1+2} &= \\
 \frac{1}{\Delta\nu} \int_{\Delta\nu} \exp \left\{ - \int [k_1(\nu)q_1(p') + k_2(\nu)q_2(p')] (dp'/G) \right\} d\nu \\
 &\neq \\
 \text{Tr}_1 \text{Tr}_2 &= \left(\frac{1}{\Delta\nu} \int_{\Delta\nu} \exp \left\{ - \int [k_1(\nu)q_1(p')] (dp'/G) \right\} d\nu \right) \\
 &\quad \left(\frac{1}{\Delta\nu} \int_{\Delta\nu} \exp \left\{ - \int [k_2(\nu)q_2(p')] (dp'/G) \right\} d\nu \right), \quad (12)
 \end{aligned}$$

or in k space,

$$\begin{aligned}
 \sum_{i=1}^N \exp \{ - [w_1 \langle k_1(g_i) \rangle + w_2 \langle k_2(g_i) \rangle] g_i \} \\
 \neq \sum_{i=1}^N \sum_{j=1}^N \exp \{ - [w_1 \langle k_1(g_i) \rangle + w_2 \langle k_2(g_j) \rangle] g_i g_j \}. \quad (13)
 \end{aligned}$$

On the left-hand side of (13) the same mapping is applied to both gases, while on the right-hand side of (13) different mappings are applied to each gas. The spectral correlation between the two gases is lost for the multiplicative result shown on the right-hand sides of (12) and (13). There are, however, two atmospheric conditions under which the inequality in (12) and (13) can

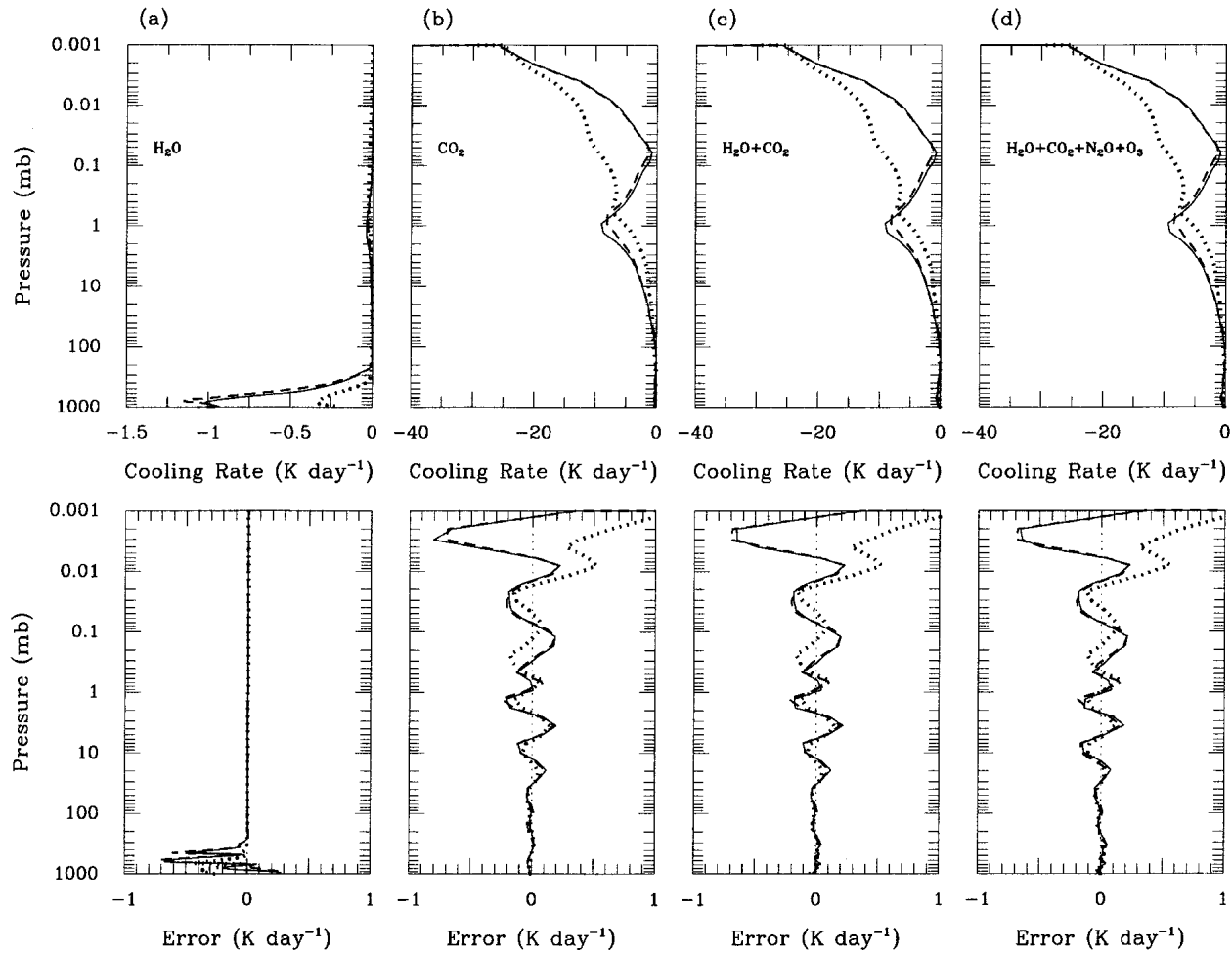


FIG. 3. Heating rate profiles and corresponding errors for (a) H_2O , (b) CO_2 , (c) $\text{H}_2\text{O} + \text{CO}_2$, and (d) $\text{H}_2\text{O} + \text{CO}_2 + \text{N}_2\text{O} + \text{O}_3$ in $540\text{--}800\text{ cm}^{-1}$. Solid lines, dashed lines, and dotted lines are for MLS, TRO, and SAW, respectively. The mixing ratio of CO_2 is 350 ppm.

become an equality. First, one of the two $k_1(\nu)$ and $k_2(\nu)$ is constant, and the proof is straightforward. But atmospheric gaseous absorption coefficients are not constant. Nevertheless, when the variation of absorption coefficient for one gas is much smaller than that for

another gas, its absorption coefficient can be approximated as constant and the equality in (12) and (13) is *approximately* true. For example, the variation of the absorption coefficient for the water vapor continuum is much smaller than that for water vapor lines. Second, if

TABLE 2. Comparisons of upward flux (W m^{-2}) in the $540\text{--}800\text{ cm}^{-1}$ band at the TOA and downward flux (W m^{-2}) at the surface for three atmospheric profiles. The numbers on the left are line-by-line results (line only), while the numbers on the right are the model results. The difference is shown in parentheses (W m^{-2}).

		H_2O		CO_2		$\text{H}_2\text{O} + \text{CO}_2$		$\text{H}_2\text{O} + \text{CO}_2 + \text{N}_2\text{O} + \text{O}_3$	
		$F^+(\text{TOA})$							
MLS	100.10	90.01 (−10.09)	74.11	73.53 (−0.58)	68.93	69.01 (0.08)	68.18	68.29 (0.09)	
TRO	103.96	92.65 (−10.31)	75.54	74.81 (−0.73)	69.00	69.01 (0.01)	68.29	68.33 (0.04)	
SAW	68.00	66.65 (−1.35)	51.99	51.87 (−0.12)	51.12	51.22 (0.10)	50.47	50.52 (0.05)	
		$F^-(\text{surface})$							
MLS	67.77	90.43 (22.65)	74.15	76.10 (1.95)	97.53	96.94 (−0.61)	97.67	97.06 (−0.61)	
TRO	79.01	100.44 (21.43)	79.46	81.49 (2.03)	105.87	105.66 (−0.21)	105.95	105.73 (−0.22)	
SAW	19.13	35.65 (16.52)	44.18	45.52 (1.34)	52.48	52.30 (−0.18)	52.97	52.71 (−0.26)	

the optical depths of one gas are much smaller than those for another gas, the proof is also straightforward.

In the case of H_2O and CO_2 in $540\text{--}800\text{ cm}^{-1}$, the interaction of the two gases is strong; thus both conditions discussed above are not valid. Since effort is made to obtain accurate $\text{Tr}_{\text{H}_2\text{O}+\text{CO}_2}$, results for $\text{Tr}_{\text{H}_2\text{O}}$ only could be poor.

Figure 3d shows results for $\text{H}_2\text{O} + \text{CO}_2 + \text{N}_2\text{O} + \text{O}_3$. The influence of N_2O and O_3 on the cooling rate is much smaller than that of H_2O or CO_2 . Hence, the simpler method, referred to as method 3, is used to solve the overlap with N_2O and O_3 .

Physically, method 1 is an exact scheme to handle the overlap of two gases. Results produced by it should be very reliable. Figure 4 depicts cooling rates for $1/2 \times$, $2 \times$, and $4 \times \text{CO}_2$. Relative errors change little compared to those for $1 \times \text{CO}_2$. Corresponding results for flux are listed in Table 3.

2) METHOD 2 (ALTERNATE MAPPING)

Besides being expensive, it is almost impossible for method 1 to handle the overlap of three or more gases. For example, in $1100\text{--}1400\text{ cm}^{-1}$ with the overlap of H_2O , N_2O , and CH_4 one needs to consider at least

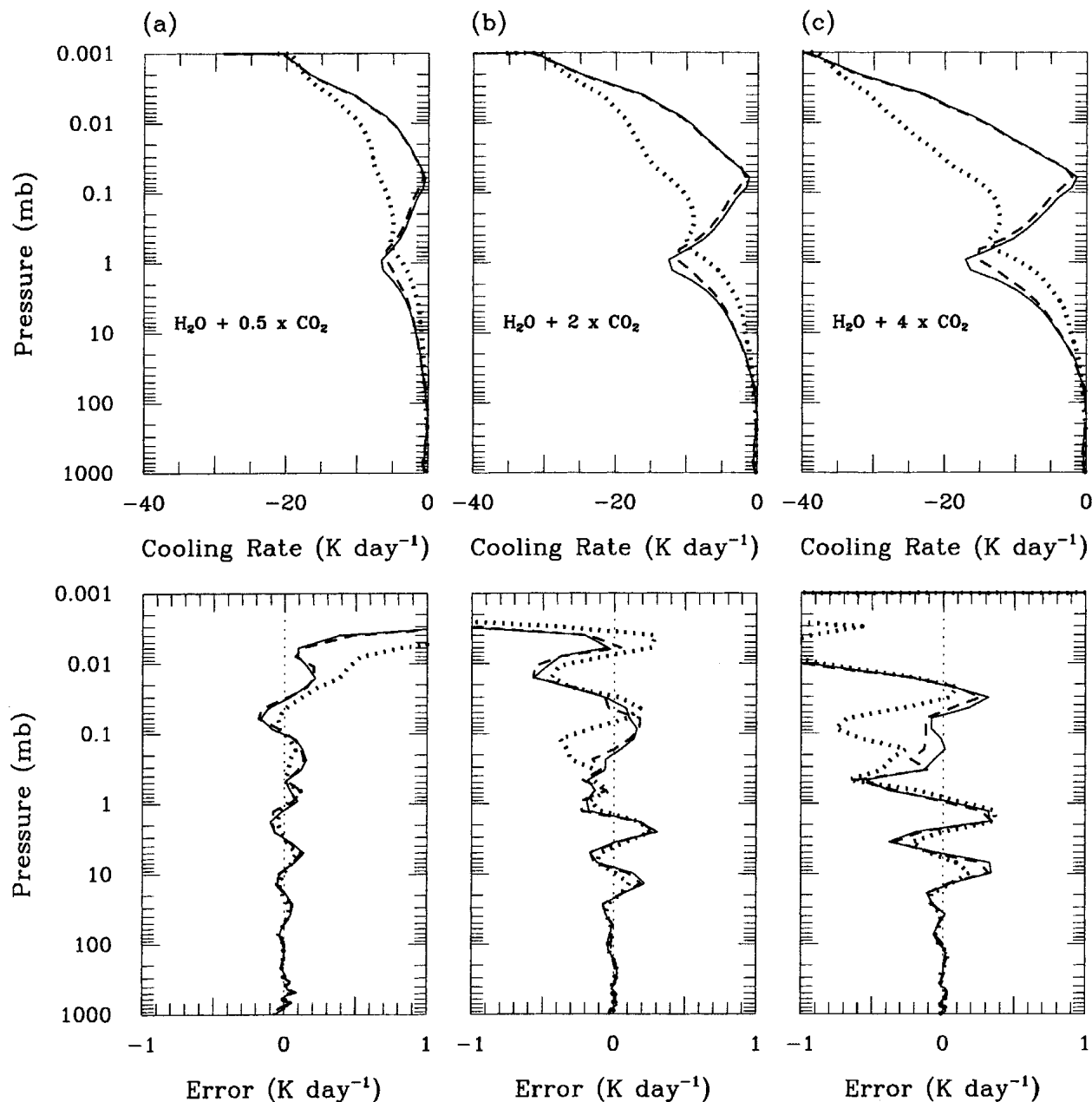


FIG. 4. Similar to $\text{H}_2\text{O} + \text{CO}_2$ in Fig. 3, but with $0.5 \times \text{CO}_2$ (175 ppm), $2 \times \text{CO}_2$ (700 ppm), and $4 \times \text{CO}_2$ (1400 ppm).

TABLE 3. The same as Table 2, but for $0.5 \times \text{CO}_2$, $2 \times \text{CO}_2$, and $4 \times \text{CO}_2$.

	$\text{H}_2\text{O} + 0.5 \times \text{CO}_2$		$\text{H}_2\text{O} + 2 \times \text{CO}_2$		$\text{H}_2\text{O} + 4 \times \text{CO}_2$	
			F^+ (TOA)			
MLS	71.85	72.06 (0.21)	66.28	66.20 (−0.08)	63.98	63.66 (−0.32)
TRO	72.31	72.44 (0.13)	65.98	65.78 (−0.20)	63.31	62.94 (−0.37)
SAW	52.84	52.94 (0.10)	49.45	49.45 (0.0)	47.96	47.82 (−0.14)
			F^- (surface)			
MLS	94.77	94.27 (−0.50)	99.95	99.84 (−0.11)	102.12	102.25 (0.13)
TRO	103.25	103.59 (0.34)	108.21	108.31 (0.10)	110.34	110.65 (0.32)
SAW	49.59	49.08 (−0.51)	54.99	55.06 (0.07)	57.11	57.85 (0.74)

three sets of interpolation to solve the mutual relations among the three gases. Here, a simple method is proposed that will be used to solve the gaseous overlap for most cases.

First, consider the case of solar radiation in $2500\text{--}4200\text{ cm}^{-1}$ where H_2O and CO_2 overlap. The interaction of the two gases is weaker than the same two gases in $540\text{--}800\text{ cm}^{-1}$. In the lower atmosphere, H_2O dominates heating, but at higher altitudes, CO_2 is dominant. This differs from the case of $540\text{--}800\text{ cm}^{-1}$, in which both H_2O and CO_2 play important roles in the lower atmosphere.

Recall that a g_i located far from 1 in CPS contributes to heating the lower atmosphere. Since H_2O plays an important role in the lower atmosphere, $k_{\text{H}_2\text{O}}(\nu, p, T)$ is sorted in CPS for $0 \leq g \leq 0.9375$, and the same sorting rules are applied to $k_{\text{CO}_2}(\nu, p, T)$ in the same interval.

Figure 5 (left panels) depicts the absorption coefficients of H_2O and CO_2 in CPS for the range of $0 \leq g \leq 0.9375$ for pressure levels of 1 and 1000 mb. Clearly, $k_{\text{H}_2\text{O}}(g, p, T)$ is well sorted in ascending order (solid line), but with the same sorting, $k_{\text{CO}_2}(\nu, p, T)$ is quite random in appearance (dashed line). Figure 5 shows that at 1000 mb the well-sorted $k_{\text{H}_2\text{O}}(g, p, T)$ are generally several orders of magnitude larger than the corresponding $k_{\text{CO}_2}(g, p, T)$. Also, in the lower atmosphere, the mass mixing ratio of H_2O greatly exceeds that of CO_2 . Thus in the lower atmosphere, the optical depth and heating rate for H_2O are much larger than those for CO_2 , and so it is important to handle heating by H_2O accurately. The use of six intervals in the range from 0 to 0.9376 leads to errors in heating rate for H_2O that are less than 0.04 K day^{-1} below 100 mb (see Fig. 6).

As discussed in section 2b(1) for a random pattern of gaseous absorption coefficients in CPS (like that for CO_2 in the left panels of Fig. 5), gaseous transmission is handled poorly by the CKD method when using only a few intervals in CPS. However, since the heating rate of CO_2 is much smaller than that of H_2O in the lower atmosphere, Fig. 6 shows that the total heating rate for $\text{H}_2\text{O} + \text{CO}_2$ is predicted accurately in the lower atmosphere below 100 mb.

Above 10 mb, CO_2 dominates heating, but the contribution by H_2O is not negligible. It was found that if the sorting for $g \geq 0.9376$ is based on $k_{\text{CO}_2}(\nu, p, T)$ only,

the heating rate by H_2O cannot be simulated accurately. Therefore, an alternate sorting is used for each gas in that CPS range. Figure 5 (middle panels) depicts the sorting pattern in the range $0.9376 \leq g \leq 0.9974$. Sorting for $0.9376 \leq g \leq 0.97605$ is based on $k_{\text{CO}_2}(\nu, p, T)$; for $0.97605 \leq g \leq 0.98975$ it is based on $k_{\text{H}_2\text{O}}(\nu, p, T)$; and for $0.98975 \leq g \leq 0.9974$ it is based on $k_{\text{CO}_2}(\nu, p, T)$ again.

At higher altitudes (see the case of 1 mb in Fig. 5), $k_{\text{H}_2\text{O}}(g, p, T)$ in the well-sorted portions is about several orders of magnitude larger than typical values of $k_{\text{H}_2\text{O}}(g, p, T)$ in the random portions. Thus, although $k_{\text{H}_2\text{O}}(g, p, T)$ is not sorted in the whole range, the dominant components of $k_{\text{H}_2\text{O}}(\nu, p, T)$ are sorted well. The same is true for CO_2 .

Alternate sorting is used in this range because if the first portion, g_9 , is too wide, many H_2O absorption lines would be gathered into g_9 in random form (the sorting is from 1 to 0 in CPS); then even with the same width of g_8 , much less useful information can be obtained for $k_{\text{H}_2\text{O}}(g, p, T)$. More alternate sorting ranges should be considered in the region very close to 1 in CPS since the variation in absorption coefficient in this region is generally much larger than that outside of it.

Figure 5 shows that although the sorted curves for H_2O are not connected, values for the two neighboring ending points are almost equal. For example, the value of g_{10} 's upper ending point is about the same as g_{12} 's lower ending point. The smooth sorted curve still exists at this point, though g_{10} and g_{12} are not connected. Of course, some information is lost in the portions where the sorting is based on CO_2 , as in g_{11} and g_{13} . However, if the alternate sorting with the proper width for each interval is used, the main feature for the sorted absorption coefficients can be approximately kept for each gas. Figure 5 (right panels) (case of 1 mb) shows that the sorted absorption coefficients are much larger than the nonsorted absorption coefficients.

As for the alternate sorting, the gaseous transmission is calculated in the same way as method 1:

$$\text{Tr}(w_{\text{H}_2\text{O}}, w_{\text{CO}_2}) = \sum_{i=1}^N \exp\{-[w_{\text{H}_2\text{O}}\langle k_{\text{H}_2\text{O}}(g_i) \rangle + w_{\text{CO}_2}\langle k_{\text{CO}_2}(g_i) \rangle]\} g_i;$$

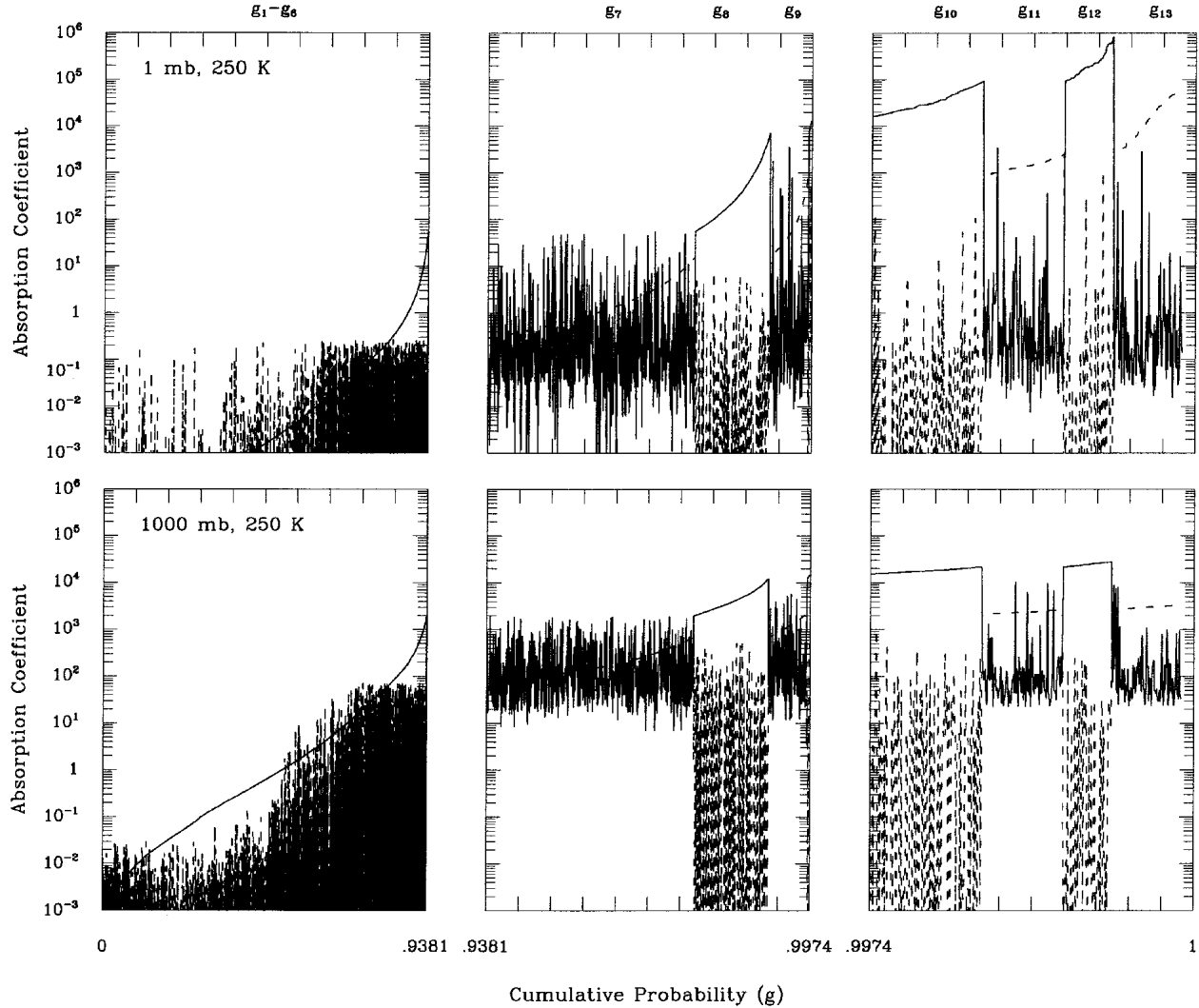


FIG. 5. Rearrangements of absorption coefficients in CPS for H_2O and CO_2 in $2500\text{--}4200\text{ cm}^{-1}$. Solid lines are for H_2O and dashed lines are for CO_2 . Two pressure levels are considered with (top) 1 and (bottom) 1000 mb. Here, g_i ($i = 1, 2, \dots, 13$) are intervals in CPS.

however, in each interval g_i , only $\langle k_{\text{H}_2\text{O}}(g_i) \rangle$ or $\langle k_{\text{CO}_2}(g_i) \rangle$ is well sorted in ascending order.

Figure 6 shows heating rates in $2500\text{--}4200\text{ cm}^{-1}$ for both H_2O only and $\text{H}_2\text{O} + \text{CO}_2$. It is found that the heating rates are well simulated for all three solar zenith angles with errors of less than 0.05 K day^{-1} below 0.1 mb .

Because of the $4.3\text{-}\mu\text{m}$ CO_2 band there are large solar heating rates above 0.1 mb . In fact, most of the heating for $4.3\text{-}\mu\text{m}$ CO_2 band appears in the infrared range of $2200\text{--}2500\text{ cm}^{-1}$. That portion of the heating is addressed by the solar-infrared interaction method (see section 5). Actually, above 0.1 mb the CO_2 non-LTE effect could be very strong for both the 4.3- and $15\text{-}\mu\text{m}$ bands. Also, the 4.3- and $15\text{-}\mu\text{m}$ bands have interactions with energy transform from the 4.3- to $15\text{-}\mu\text{m}$ bands. This non-LTE effect will be discussed

in Part II (Fomichev and Li 2005, unpublished manuscript).

Now, consider a more complicated case of $1100\text{--}1400\text{ cm}^{-1}$ in the infrared with three major gases: H_2O , N_2O , and CH_4 . Heating rates depicted in Fig. 7 show that in the region above 0.1 mb , cooling by CH_4 dominates. Thus, the sorting in $0.98 \leq g \leq 1$ is based on $k_{\text{CH}_4}(\nu, p, T)$. The relatively large heating rates for N_2O occur near 1 mb , and so sorting from $0.93 \leq g \leq 0.98$ is based on $k_{\text{N}_2\text{O}}(\nu, p, T)$. In the lower atmosphere, H_2O dominates heating and so sorting in $0 \leq g \leq 0.93$ is based on $k_{\text{H}_2\text{O}}(\nu, p, T)$. Figure 8 presents results for these sortings for pressure levels of 1 and 1000 mb. In Fig. 8 (bottom-left panel) the average absorption coefficients for N_2O and CH_4 could be about two orders of magnitude larger than the sorted H_2O absorption coefficient. However, in the lower atmosphere the mass mixing ratio of H_2O

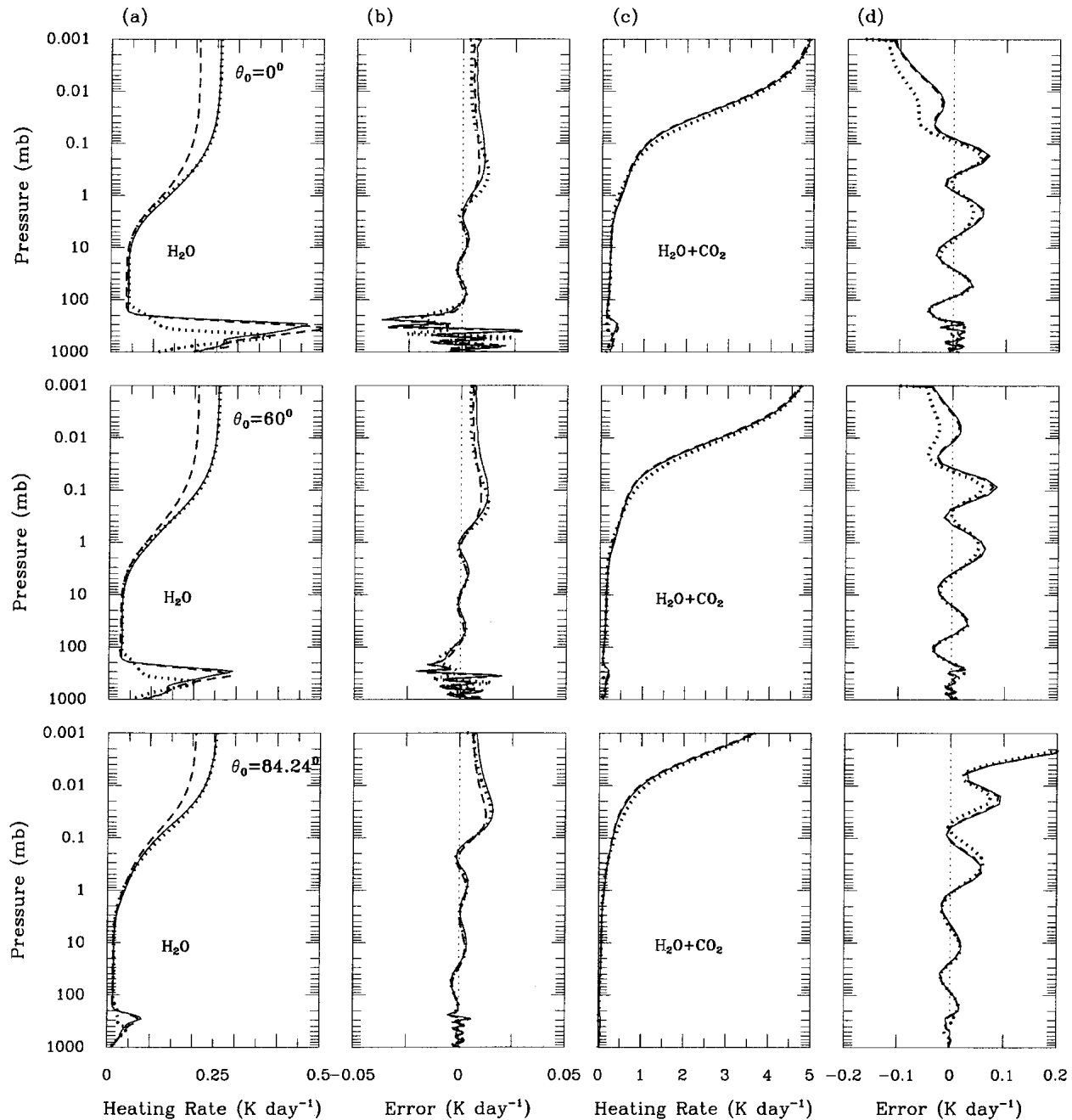


FIG. 6. Solar heating rates and model errors in $2500\text{--}4200\text{ cm}^{-1}$. (a) Solar heating rates by H_2O only, (b) corresponding model errors, (c) solar heating rates for $\text{H}_2\text{O} + \text{CO}_2$, and (d) corresponding model errors. Solid lines, dashed lines, and dotted lines are for MLS, TRO, and SAW, respectively. The mixing ratio of CO_2 is 350 ppm.

is about two to four orders of magnitude larger than that for N_2O and CH_4 . As such, cooling is dominated by H_2O in the lower atmosphere. Heating rates for H_2O , N_2O , CH_4 , and $\text{H}_2\text{O} + \text{N}_2\text{O} + \text{CH}_4$ are shown in Fig. 7. As expected, the cooling rates of H_2O alone are well simulated in lower atmosphere, and cooling rates for N_2O and CH_4 are much smaller compared to those for H_2O . The relative errors in the heating rate for N_2O

and CH_4 are not small in the lower atmosphere since the transmission cannot be handled accurately with a few intervals in CPS for absorption coefficients with random patterns. However, since the effects of N_2O and CH_4 are weak in the lower atmosphere, results in the cooling rate for $\text{H}_2\text{O} + \text{N}_2\text{O} + \text{CH}_4$ are about as accurate as for pure H_2O . Figure 8 (top panels) shows that the N_2O absorption coefficients in the sorted por-

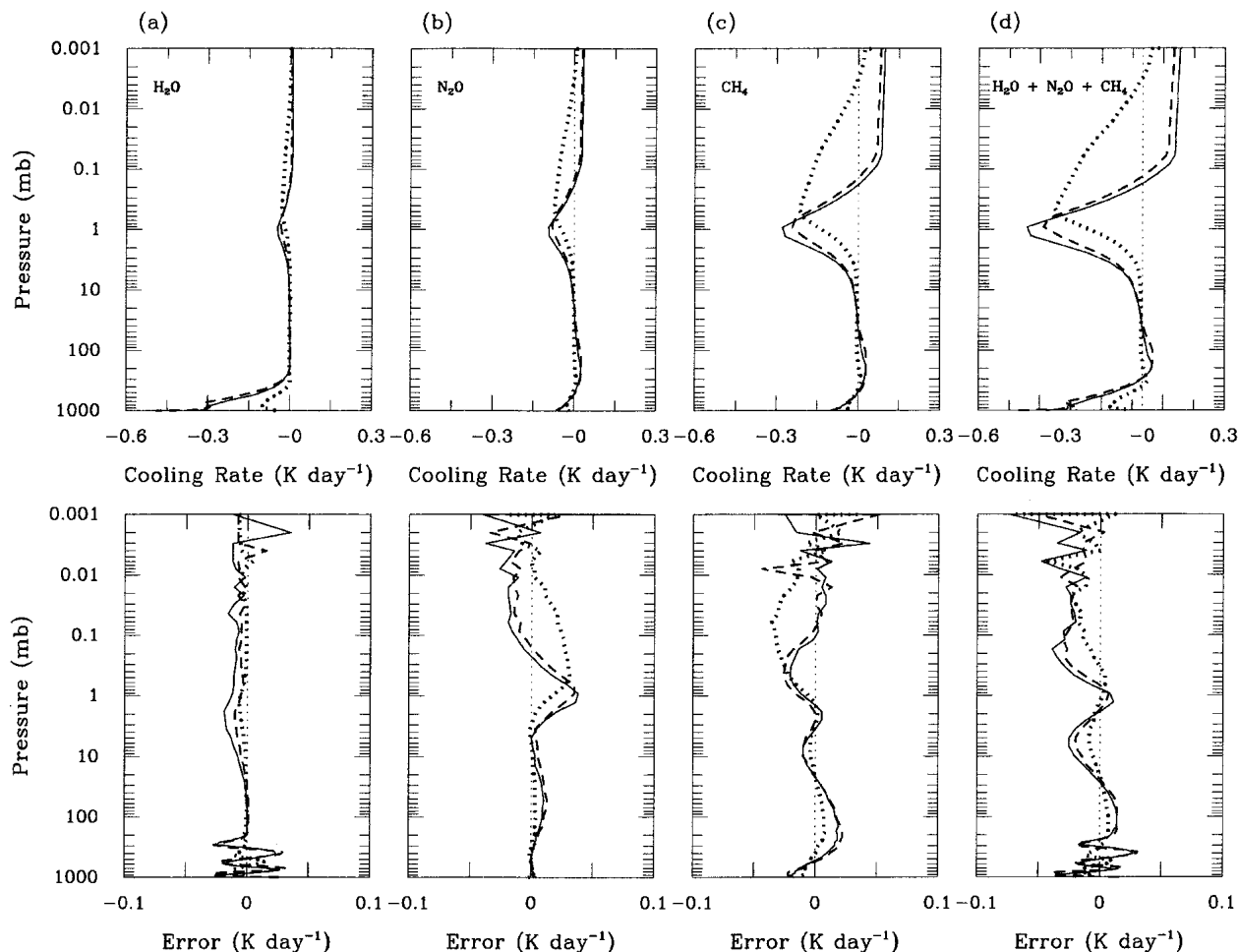


FIG. 7. Heating rate profiles and corresponding errors for H_2O , N_2O , CH_4 , and $\text{H}_2\text{O} + \text{N}_2\text{O} + \text{CH}_4$ in $1100\text{--}1400\text{ cm}^{-1}$; solid, dashed, and dotted lines as in Fig. 3.

tion are much larger than those in the nonsorted (random) portion. The same is true for CH_4 . As discussed above, the useful information resides in the sorted portion, and errors in the heating rates for N_2O and CH_4 could be small if a proper number of intervals in CPS is applied. Corresponding fluxes and their errors are listed in Table 4.

Another case in need of discussion is H_2O and O_3 in $980\text{--}1100\text{ cm}^{-1}$ where O_3 cooling is important in the infrared. The ranges of $0 \leq g \leq 0.933$ and $0.973 \leq g \leq 1$ are sorted based on $k_{\text{O}_3}(\nu, p, T)$ with a total of five intervals, and $0.933 \leq g \leq 0.973$ based on $k_{\text{H}_2\text{O}}(\nu, p, T)$ with only one interval since cooling by H_2O is very small, even in the lower atmosphere. Cooling rate and corresponding errors for H_2O , O_3 , and $\text{H}_2\text{O} + \text{O}_3$ are shown in Fig. 9, and flux results are listed in Table 5.

In the near-infrared and infrared ranges (without $540\text{--}800\text{ cm}^{-1}$), H_2O is the dominant gas in the lower atmosphere. By method 2, most bands in the first few intervals of CPS, which usually covers the range from 0 to > 0.9 in CPS, are based on sorting of H_2O . In

$980\text{--}1100\text{ cm}^{-1}$ H_2O and O_3 are the exceptions, as the effect of H_2O in this range is very small. Therefore, results for H_2O are simulated well in the near-infrared and infrared. At the same time, optical depths for other gases in the lower atmosphere are generally much smaller than that for H_2O . Following the discussion in section 2b(1), $\text{Tr}_{\text{H}_2\text{O}+2+3+\dots} \approx \text{Tr}_{\text{H}_2\text{O}}\text{Tr}_{2+3+\dots}$, where $\text{Tr}_{2+3+\dots}$ refers to transmittance by other gases. Higher in the atmosphere, the situation is usually reversed: optical depths are very small for H_2O and $\text{Tr}_{\text{H}_2\text{O}+2+3+\dots} \approx \text{Tr}_{\text{H}_2\text{O}}\text{Tr}_{2+3+\dots}$ is also true. Thus in principle, for the near-infrared and infrared (without $540\text{--}800\text{ cm}^{-1}$), H_2O alone and in combination with all other gases are handled accurately by method 2 (see section 3).

3) METHOD 3 (SIMPLE FORCING ADJUSTMENT)

Some gases play a very weak role in atmospheric heating, but have a small yet noticeable effect on net flux at the surface and the TOA: for example, N_2O in $1900\text{--}2200\text{ cm}^{-1}$, O_3 in $540\text{--}800$ and $8400\text{--}14\,500\text{ cm}^{-1}$, and O_2 in $14\,500\text{--}50\,000\text{ cm}^{-1}$, etc. These gases are

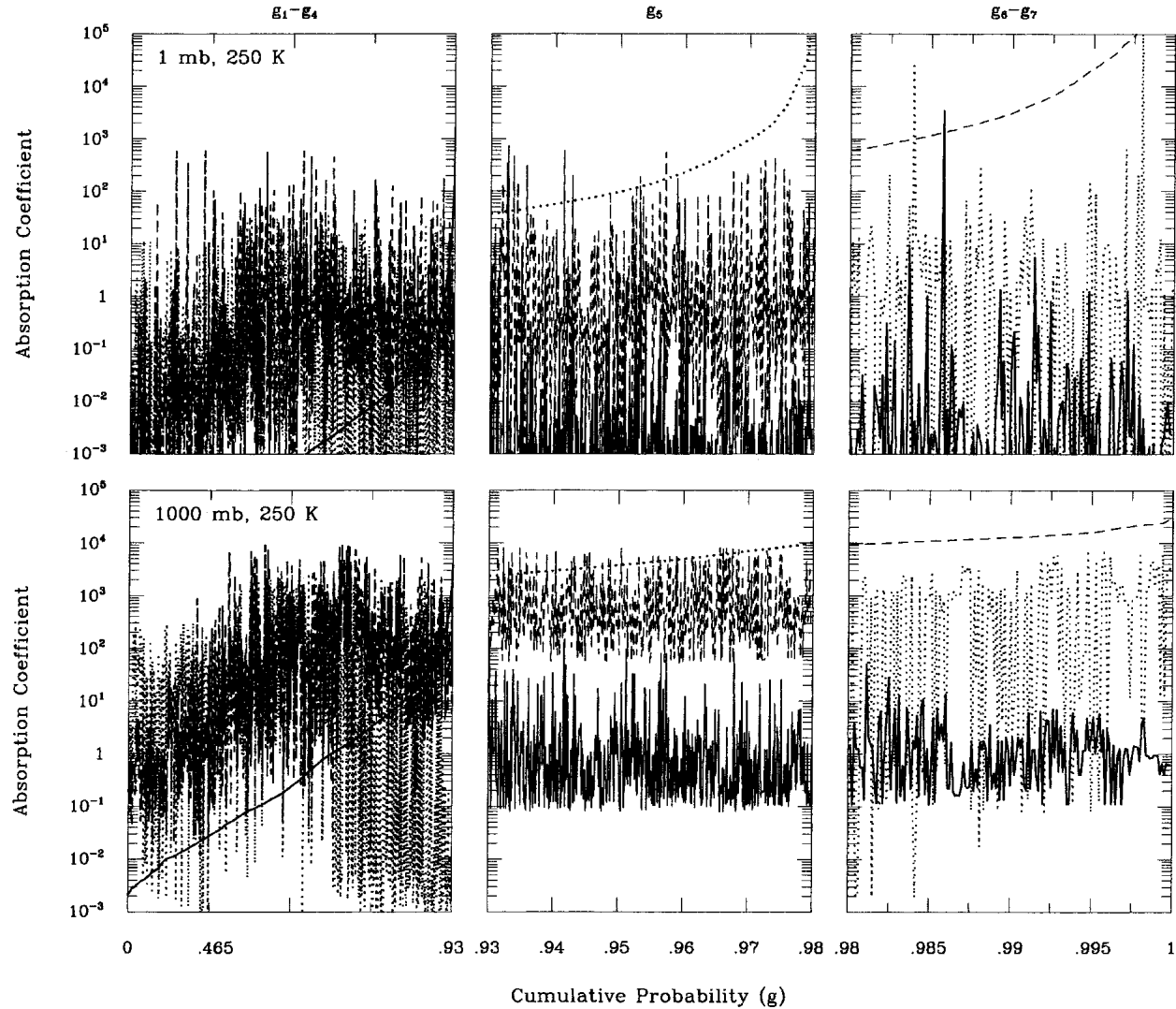


FIG. 8. Rearrangements of absorption coefficients in CPS for H_2O , N_2O , and CH_4 in $1100\text{--}1400\text{ cm}^{-1}$. Solid lines are for H_2O , dashed lines are for CH_4 , and dotted lines are for N_2O . Two pressure levels are considered with (top) 1 and (bottom) 1000 mb. Here, g_i ($i = 1, 2, \dots, 13$) are intervals in CPS.

called minor gases here. For minor gases there is no need to use the complicated methods shown above to deal with the gaseous transmission. We need only fit their transmission functions roughly by treating them as

gray gases that are independent of temperature and pressure. To simplify matters further, it is not necessary to consider transmission for all g_i in CPS, but only apply it to the first few g_i ($i = 1, 2, \dots$) since the contribution

TABLE 4. In $1100\text{--}1400\text{ cm}^{-1}$, the comparisons of upward flux (W m^{-2}) at the TOA and downward flux at the surface for three atmospheric profiles. The numbers on the left are the line-by-line results (line only); the numbers on the right are the model results. The difference is shown in parentheses (W m^{-2}).

		H ₂ O		N ₂ O		CH ₄		H ₂ O + N ₂ O + CH ₄	
		F ⁺ (TOA)							
MLS	38.50	38.61 (0.11)	46.30	46.52 (0.22)	44.67	44.38 (−0.29)	34.70	34.98 (0.28)	
TRO	41.41	41.62 (0.21)	52.05	52.31 (0.26)	50.10	49.76 (−0.34)	37.32	37.74 (0.42)	
SAW	19.40	19.26 (−0.14)	19.83	19.88 (0.05)	19.35	19.25 (−0.10)	17.58	17.39 (−0.17)	
		F [−] (surface)							
MLS	27.24	27.27 (0.03)	3.92	3.38 (−0.44)	6.31	6.62 (0.31)	28.90	28.85 (−0.05)	
TRO	33.18	32.95 (−0.23)	4.28	3.67 (−0.61)	6.97	7.20 (0.23)	34.55	34.25 (−0.30)	
SAW	6.30	6.62 (0.32)	1.86	1.69 (−0.17)	2.83	3.25 (0.42)	8.49	8.97 (0.48)	

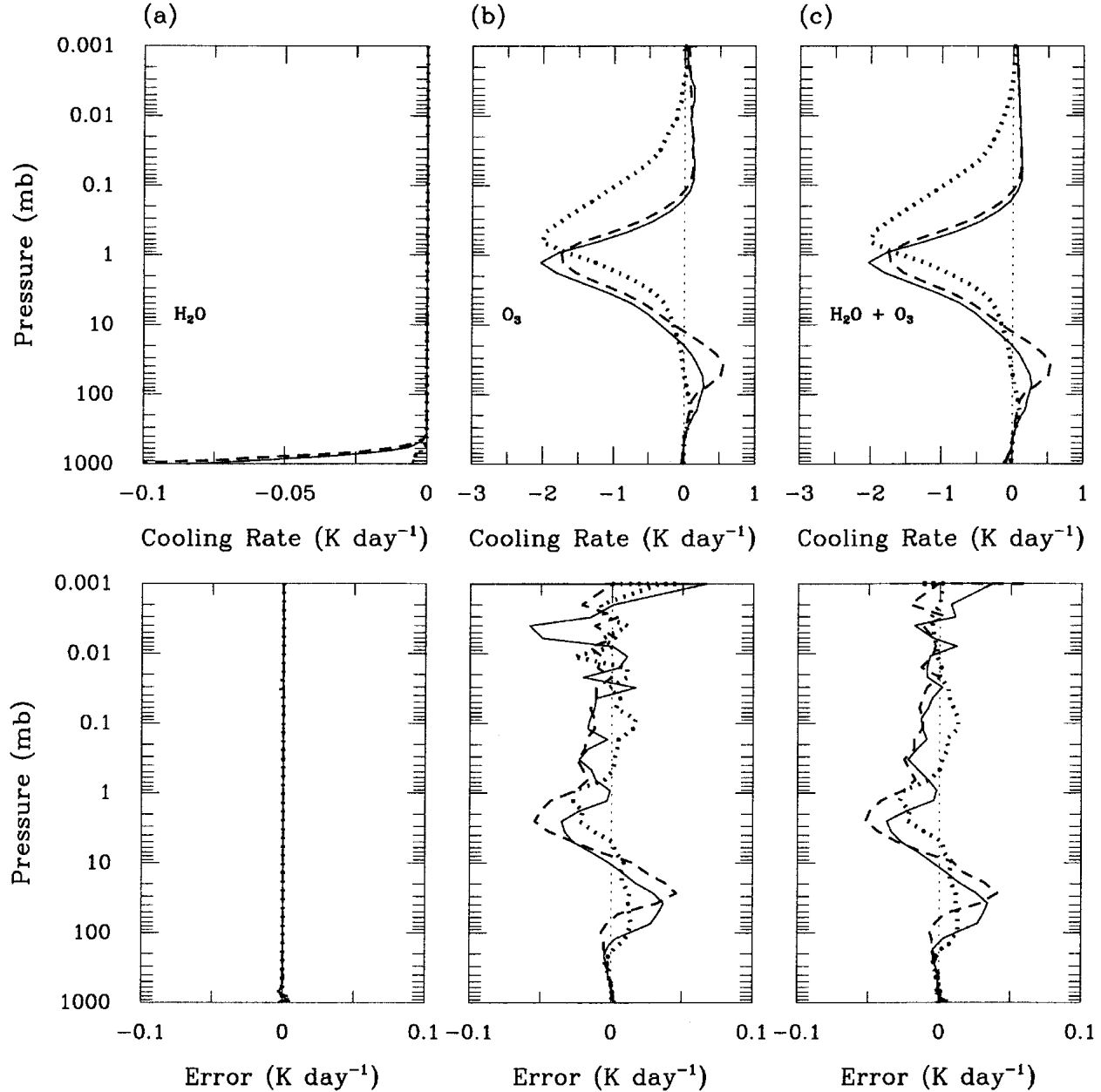


FIG. 9. Heating rate profiles and corresponding errors for H_2O , O_3 , and $\text{H}_2\text{O} + \text{O}_3$ in $980\text{--}1100\text{ cm}^{-1}$. Solid, dashed, and dotted lines as in Fig. 3.

by the remaining part of g_i is negligible in the weak gas case. Thus,

$$\text{Tr}_{\text{minor}} = \sum_{i=1}^n \exp[-\langle k \rangle_i q \Delta p / G] g_i, \quad (14)$$

where Tr_{minor} is the transmission function for the minor gas calculation; q is the scaled absorber amount; Δp is the pressure difference; $\langle k \rangle_i$ is absorption coefficient for interval g_i ; and $n \leq N$, where N is the total interval number in CPS for the considered band. Since the ef-

fect of a minor gas is very small, its interaction with other gases is weak. Thus, overlap involving a minor gas is treated as $\text{Tr}_{\text{minor}+\text{main}} = \text{Tr}_{\text{minor}} \text{Tr}_{\text{main}}$. This simple method is sufficient for weak gases as illustrated by results in section 3.

c. Continuum

The Atmospheric Environmental Research (AER) continuum scheme (CKD 2.4; Mlawer et al. 1997) is used. Only the continuum for water vapor in the infra-

TABLE 5. In $980\text{--}1100\text{ cm}^{-1}$, the comparisons of upward flux (W m^{-2}) at the TOA and downward flux at the surface for three atmospheric profiles. The numbers on the left are the line-by-line results (line only); the numbers on the right are the model results. The difference is shown in parentheses (W m^{-2}).

	H_2O		O_3		$\text{H}_2\text{O} + \text{O}_3$	
			$F^+(\text{TOA})$			
MLS	30.90	30.89 (−0.01)	23.04	23.01 (−0.03)	22.77	22.75 (−0.02)
TRO	33.97	33.96 (−0.01)	26.52	26.67 (0.15)	26.52	26.67 (0.15)
SAW	15.07	15.08 (0.01)	11.02	10.86 (−0.16)	11.01	10.85 (−0.16)
			$F^-(\text{Surface})$			
MLS	2.66	2.64 (−0.02)	4.41	4.20 (−0.21)	6.58	6.38 (−0.20)
TRO	3.76	3.76 (0.00)	6.85	6.64 (−0.21)	6.85	6.64 (−0.21)
SAW	0.20	0.20 (0.00)	2.82	2.83 (0.01)	2.98	2.98 (0.0)

red is considered. First, the continuum is set to match line-by-line calculations with a spectral line wing cutoff of 25 cm^{-1} . The water vapor continuum spectra are sorted in the same way as the water vapor line spectra for each band. Also, the intervals in CPS for water vapor continuum are the same as those for the corresponding water vapor lines. However, it was found that the effect of the water vapor continuum for some intervals in CPS is very small. These intervals are generally very close to 1 in CPS since absorption lines in these intervals are so sharp that what extends beyond the 25-cm^{-1} cutoff is very small. Table 1 shows the number of intervals in each band for which water vapor continuum is addressed; about half the calculations can be avoided. In Table 1, the definition of major and minor intervals in CPS is discussed in section 4.

Moreover, the water vapor continuum is applied only from the surface to an upper level that varies from 300 to 100 mb depending on the line sharpness. Limiting the continuum to the lower atmosphere makes the radiation model more efficient.

As mentioned, the interaction of water vapor and CO_2 is very strong in $540\text{--}800\text{ cm}^{-1}$. Thus, method 1 is used to handle the gaseous overlap with five reference values for the ratio of water vapor to CO_2 . However, the variation in absorption coefficient for the water vapor continuum is much smaller than that for the water vapor lines. Just two reference values of $r = 0.01$ and $r = 16$ can generate accurate results for heating rates and fluxes with the water vapor continuum included.

3. Results

a. Visible $14\,500\text{--}50\,000\text{ cm}^{-1}$ with O_3 , O_2 , and H_2O

In the visible range O_3 dominates the heating rate. The O_3 absorption coefficient given in WMO (1996) was used to calculate the benchmark results by dividing the visible range into 355 000 narrow bands. We parameterize the O_3 model absorption coefficient into nine subbands with UVC, UVB, UVA, and photosynthetic active radiation (PAR) separately considered (see Table 6). One subband contains parts of UVB and UVA, because we split UVA at $32\,185\text{ cm}^{-1}$ for the J value. The solar photon energy between $32\,185$ and $50\,000\text{ cm}^{-1}$ is important for kinetic energy, chemical potential energy to destroy O_3 , and internal energy of the photodissociation products. This spectral range has to be distinguished by the spectral cut at $32\,185\text{ cm}^{-1}$ called the J value. It is shown in Fig. 10 that the model can produce very accurate results even with only nine subbands for the cases of three atmospheric profiles and with three solar zenith angles θ_0 of 0° , 60° , and 84.24° ($\cos \theta_0 = 1, 0.5$, and 0.1). Errors are always smaller than 0.2 W m^{-2} .

Heating by O_2 in $41\,254\text{--}50\,000\text{ cm}^{-1}$ (Herzberg continuum) cannot be ignored above 10 mb. We simply parameterize the O_2 absorption coefficient in subband 1. The O_2 Schumann–Runge band is located mostly in $50\,000\text{--}57\,600\text{ cm}^{-1}$. Though incoming solar energy in this range is only about 0.3 W m^{-2} , the heating rate can

TABLE 6. In visible $14\,500\text{--}50\,000\text{ cm}^{-1}$, the subband spectrum ranges, absorber, and the absorption coefficients for O_3 and solar subband weight. The ranges of UVA, UVB, UVC, and PAR and J value are listed.

Subband	Spectral range (cm^{-1})		Absorber	Absorption coefficient ($\text{cm}^2\text{ g}^{-1}$) O_3	Solar weight (W m^{-2})
1	50 000–42 000	UVC	O_3 , ray, O_2	47 069.968 75	1.571 22
2	42 000–37 400	UVC	O_3 , ray	129 469.968 75	2.788 22
3	37 400–35 700	UVC	O_3 , ray	82 530.031 25	2.784 86
4	35 700–34 000	UVB	O_3 , ray	19 933.671 88	5.542 84
5	34 000–32 185	UVB, UVA	O_3 , ray	3410.008 30	9.711 53
6	32 185–30 300	UVA, J value: 32 185	O_3 , ray	306.996 03	16.033 34
7	30 300–25 000	UVA	O_3 , ray	4.050 37	73.073 72
8	25 000–20 000	PAR	O_3 , ray	4.283 15	187.186 23
9	20 000–14 500	PAR	O_3 , ray H_2O , O_2	37.313 82	330.385 62

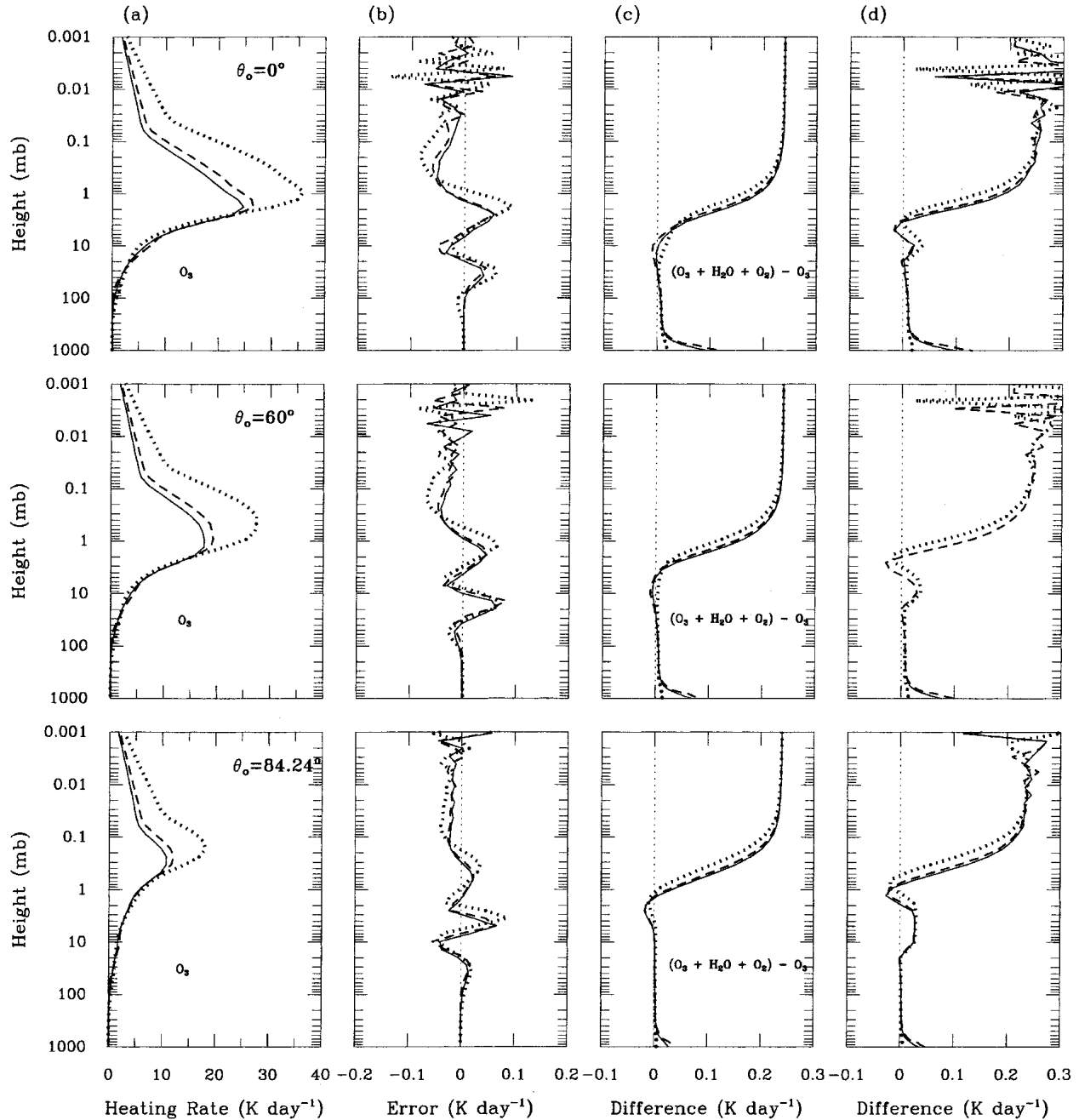


FIG. 10. Solar heating rates and model errors in the visible range ($14\,500\text{--}50\,000\text{ cm}^{-1}$). (a) Solar heating rates by O_3 and (b) corresponding model errors. (c) Benchmark results of the difference between heating rates by $\text{O}_3 + \text{O}_2 + \text{H}_2\text{O}$ and by O_3 . (d) Same as (c) but for model simulations. Solid, dashed, and dotted lines as in Fig. 3.

be over 10 K day^{-1} above 0.1 mb . The Schumann–Runge band is ignored in this model but can be accounted for easily by Strobel’s (1978) parameterization.

In the visible $14\,500\text{--}20\,000\text{ cm}^{-1}$, O_2 and H_2O are considered by simple parameterizations based on method 3 for overlap to the main gas O_3 . Our parameterizations produce accurate results compared to

benchmark results. Figure 10c shows differences in heating rates for $\text{O}_3 + \text{O}_2 + \text{H}_2\text{O}$ minus those for O_3 . Figure 10d shows corresponding model results.

Results for upward flux at the TOA and the downward flux at surface are listed in Table 7. Errors are generally very small ($<1\text{ W m}^{-2}$) with relative errors less than 1%. In the visible range, subbands are used

TABLE 7. Comparisons of upward flux (W m^{-2}) for the visible 14 500–50 000 cm^{-1} at the TOA and downward flux (W m^{-2}) at the surface for three atmospheric profiles. The numbers on the left are line-by-line results, and numbers on the right are model results. Differences are shown in parentheses (W m^{-2}). Three solar zenith angles are shown with O_3 only and $\text{O}_3 + \text{O}_2$.

	$\theta_0 = 0^\circ$				$\theta_0 = 60^\circ$				$\theta_0 = 84.24^\circ$			
	$F^+(\text{TOA})$		$F^-(\text{surface})$		$F^+(\text{TOA})$		$F^-(\text{surface})$		$F^+(\text{TOA})$		$F^-(\text{surface})$	
						O_3						
MLS	114.50	114.50 (0.0)	595.63	595.25 (−0.38)	56.25	56.24 (−0.01)	291.54	291.53 (−0.01)	9.94	9.91 (−0.03)	51.15	51.04 (−0.11)
TRO	115.90	115.90 (0.0)	598.86	598.48 (−0.38)	57.12	57.12 (0.0)	294.13	294.06 (−0.07)	10.33	10.31 (−0.02)	52.88	52.80 (−0.08)
SAW	111.55	111.51 (−0.04)	588.98	588.79 (−0.09)	54.41	54.36 (−0.05)	286.09	286.11 (0.02)	9.15	9.11 (−0.04)	47.62	47.45 (−0.07)
						$\text{O}_3 + \text{H}_2\text{O} + \text{O}_2$						
MLS	113.25	113.00 (−0.25)	592.81	592.65 (−0.16)	55.49	55.32 (−0.17)	289.19	289.13 (−0.06)	9.68	9.63 (−0.05)	49.93	49.79 (−0.14)
TRO	114.32	113.92 (−0.40)	595.33	595.09 (−0.24)	56.16	55.92 (−0.24)	291.16	290.92 (−0.24)	10.00	9.91 (−0.09)	51.31	51.07 (−0.24)
SAW	111.07	110.90 (−0.17)	587.73	587.76 (0.03)	54.12	54.00 (−0.12)	285.14	285.16 (0.02)	9.07	9.02 (−0.05)	47.20	47.06 (−0.14)

instead of g intervals because the problem is solved in frequency space, not in CPS. The subbands are determined by separating out UVA, UVB, UVC, PAR, and the J value.

b. Near-infrared 2500–14 500 cm^{-1} with H_2O , CO_2 , O_3 , and O_2

Water dominates heating in the lower atmosphere in the near-infrared range. The near-infrared is split into three bands and the CKD method is applied to each band. The numbers of intervals in CPS are listed in Table 1. First, consider H_2O only. Results for H_2O in 2500–4200 cm^{-1} have been discussed in Fig. 6. Overall heating rate for H_2O in 2500–14500 cm^{-1} is shown in Fig. 11. Errors in heating rate shown in Figs. 6 and 11 are very similar, meaning that errors in the range outside 2500–4200 cm^{-1} are small.

We use method 3 to simply include the effect of O_2 and O_3 in the near-infrared range. The total heating rates and model errors for the four gases are presented in Fig. 11. It is shown that errors in heating rate are mostly limited to within 0.2 K day^{-1} . Corresponding errors in fluxes at the TOA and the surface are listed in Table 8.

In the above calculations for visible and near-infrared, Rayleigh scattering is neglected. This is because benchmark results for Rayleigh scattering could only be obtained through a doubling–adding process with very fine vertical resolution. Benchmark results for line-by-line plus doubling–adding processes are extremely time consuming. This has only been done in the Geophysical Fluid Dynamics Laboratory (GFDL) model (Ramaswamy and Freidenreich 1991; Freidenreich and Ramaswamy 1999). This raises the question: How accurate is the model with Rayleigh scattering considered? WMO (1985) provides Rayleigh scattering coefficients σ_R for a resolution of 20 cm^{-1} . The Rayleigh optical depth for a layer of thickness dz is

$\sigma_R(A/M_a)\rho dz$, where A is Avogadro's number, M_a is molecular weight of air, and ρ is air density in the layer. Following Eq. (B7) (see appendix B) the Rayleigh scattering coefficient for each band (subband) should not simply be the band-(subband) averaged results, as generally α in (B7) is less than 1. Since the model produces accurate results for radiative transfer without Rayleigh scattering, very fine resolution Rayleigh scattering is used as a benchmark. In calculations with the full scattering process, the Rayleigh scattering coefficient is interpolated to 0.1- cm^{-1} resolution and applied to each subband. Though this is not perfect line-by-line plus Rayleigh scattering, results should be very accurate since the Rayleigh scattering coefficient is extremely smooth compared to gaseous absorption coefficients. Finally, the Rayleigh scattering coefficients for each subband can be obtained easily by adjusting α in (9) to match the benchmark results. Errors for fluxes at the surface and the TOA are less than 0.1 W m^{-2} .

It is also interesting to compare the model results with GFDL benchmark calculations. In GFDL, line-by-line plus doubling–adding calculations, the solar spectrum is from 0 to 57 600 cm^{-1} . In our model, solar radiation in the range 0–2500 cm^{-1} is treated as infrared (see section 5). In the infrared region, pure solar results can be obtained by letting the Planck function and surface emissivity be zero. Table 9 shows the results of flux and atmospheric absorption with Rayleigh scattering included. The model input conditions are set the same as the GFDL benchmark calculations. For most cases, our model is closer to GFDL benchmark results than is the model presented by Freidenreich and Ramaswamy (1999). Much of the difference between our model and the GFDL benchmark could possibly be due to the spectral line wing cutoff being just 10 cm^{-1} for the benchmark. Also, differences in the vertical resolution of atmospheric profiles and spectrum range, as well

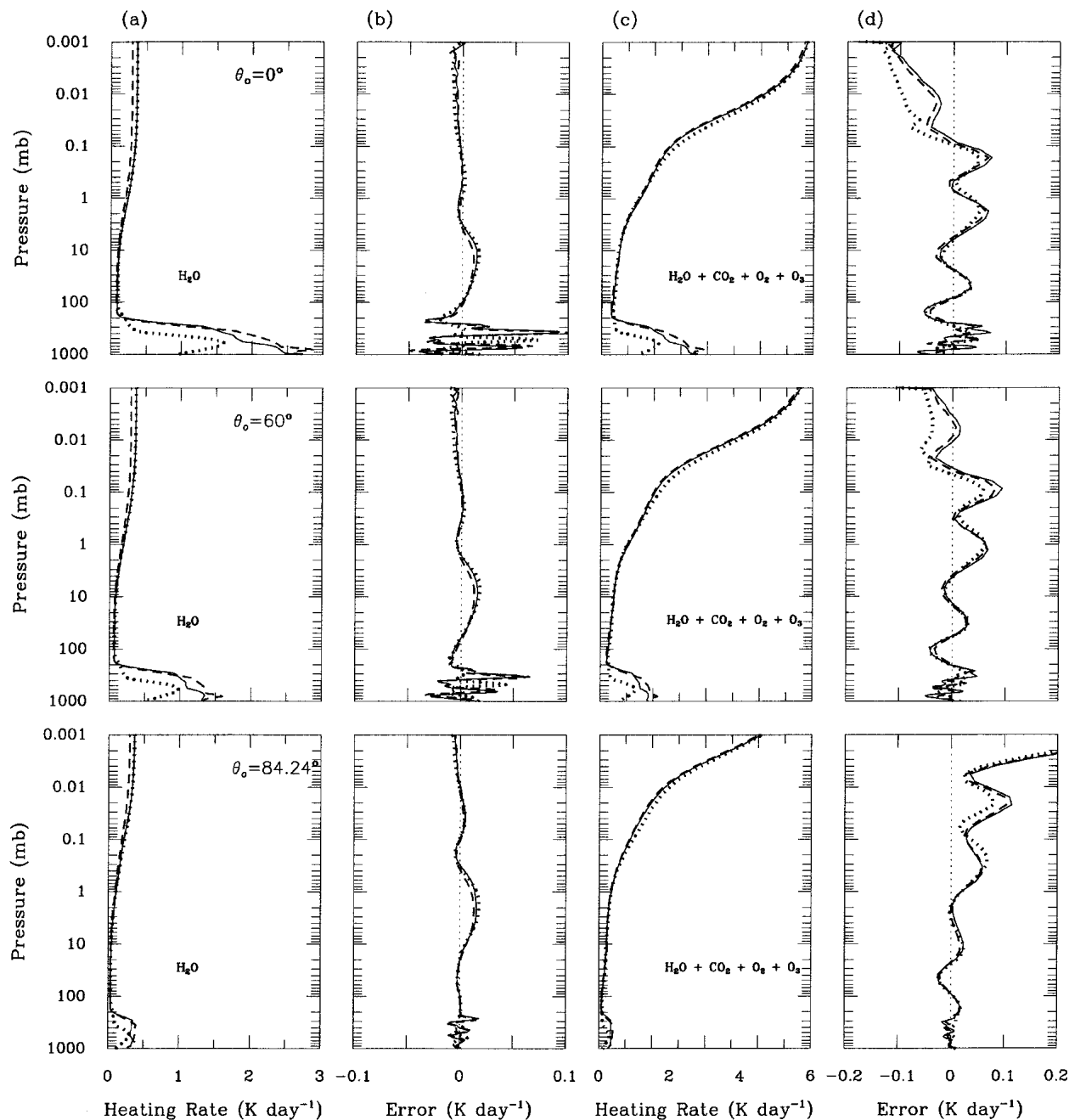


FIG. 11. Solar heating rates and model errors in the near-infrared range ($2500\text{--}14\,500\text{ cm}^{-1}$). (a) Solar heating rates by H_2O only and (b) corresponding model errors. (c) Solar heating rates by $\text{H}_2\text{O} + \text{CO}_2 + \text{O}_3 + \text{O}_2$, and (d) corresponding model errors. Solid, dashed, and dotted lines as in Fig. 3. The mixing ratio of CO_2 is 350 ppm.

as the two-stream approximation used in our model, can all cause differences in flux estimates.

c. The infrared $0\text{--}2500\text{ cm}^{-1}$ with H_2O , CO_2 , O_3 , N_2O , and CH_4

As mentioned in section 2b(1), method 1 yields accurate results for $\text{H}_2\text{O} + \text{CO}_2$ and CO_2 alone in $540\text{--}800\text{ cm}^{-1}$, but results for H_2O alone are very poor,

especially for flux. Therefore, only results for H_2O alone from all bands in the infrared except $540\text{--}800\text{ cm}^{-1}$ are summarized. Heating rates by H_2O alone are depicted in Fig. 12 with line only and line plus continuum. Corresponding results for fluxes are listed in Table 10. It is found that heating-rate errors are limited to 0.2 K day^{-1} , and errors in fluxes at the TOA and the surface are smaller than 0.5 W m^{-2} .

TABLE 8. Comparisons of upward flux (W m^{-2}) for the near-infrared 2500–14 500 cm^{-1} for upward flux (W m^{-2}) at the TOA and downward flux (W m^{-2}) at the surface for three atmospheric profiles. The numbers on the left are the line-by-line results, the numbers on the right are model results. Differences are shown in parentheses (W m^{-2}). Three solar zenith angles are shown with H_2O only, and $\text{H}_2\text{O} + \text{CO}_2 + \text{O}_2 + \text{O}_3$.

	$\theta_0 = 0^\circ$				$\theta_0 = 60^\circ$				$\theta_0 = 84.24^\circ$			
	$F^+(\text{TOA})$		$F^-(\text{surface})$		$F^+(\text{TOA})$		$F^-(\text{surface})$		$F^+(\text{TOA})$		$F^-(\text{surface})$	
	H_2O											
MLS	98.33	98.21	548.94	548.78	47.46	47.39	256.61	256.47	8.12	8.12	41.77	41.75
		(−0.12)		(−0.16)		(−0.07)		(−0.14)		(−0.00)		(−0.02)
TRO	94.13	94.00	530.85	530.74	45.30	45.24	246.30	246.18	7.66	7.65	39.46	39.44
		(−0.13)		(−0.11)		(−0.06)		(−0.12)		(−0.01)		(−0.02)
SAW	117.95	117.80	629.33	629.12	57.74	57.68	302.55	302.17	10.49	10.48	53.38	53.35
		(−0.15)		(−0.21)		(−0.06)		(−0.38)		(−0.01)		(−0.03)
	$\text{H}_2\text{O} + \text{CO}_2 + \text{O}_2 + \text{O}_3$											
MLS	95.51	95.86	539.83	540.57	45.89	46.07	250.55	251.36	7.67	7.66	39.61	39.70
		(0.35)		(0.74)		(0.18)		(0.81)		(−0.01)		(−0.09)
TRO	91.46	91.66	522.10	522.52	43.82	43.91	240.80	241.35	7.24	7.19	37.48	37.37
		(0.20)		(0.42)		(0.09)		(0.55)		(−0.05)		(−0.09)
SAW	114.57	114.65	618.85	619.47	55.84	55.86	295.41	295.67	9.89	9.80	50.59	50.29
		(0.08)		(0.62)		(0.02)		(0.26)		(−0.09)		(−0.30)

The heating rates by $\text{H}_2\text{O} + \text{CO}_2 + \text{O}_3 + \text{N}_2\text{O} + \text{CH}_4$ in 0–2500 cm^{-1} are shown in Fig. 12 with lines only and lines plus continuum. Errors in the upper atmosphere are much larger than those for H_2O alone. This is due to too few intervals for CO_2 as discussed in section 2b(1). Below 0.01 mb, errors for all five gases together are slightly larger than those for H_2O only. Notice that the H_2O continuum is handled accurately and errors for lines plus continuum are similar to errors for lines only. Corresponding errors in fluxes at the TOA and the surface are listed in Table 10.

In the infrared, with the exception of a few cases discussed in section 2, in which methods 1 and 2 were used for gaseous overlap, most of the gases are considered minor, so method 3 is used to deal with gaseous overlap. For example, in 540–800 cm^{-1} , N_2O and O_3 are treated as minor gases and simply overlapped with the main gases H_2O and CO_2 . It is found that O_3 can contribute about 0.4 K day^{-1} to the cooling rate near 1 mb. The cooling rate by N_2O in 540–800 cm^{-1} is neg-

ligible, but could have forcing at the TOA of about 0.4 W m^{-2} . Both O_3 and N_2O in 540–800 cm^{-1} have been ignored in most other models. We can easily include the effects of most of the minor gases via the efficiency of method 3.

CFC11 and CFC12 are not included in Fig. 12 and Table 10 because their effects are too small. If they are considered together with other gases, it is difficult to show how accurately they are handled by the model. The impact of CFC11 and CFC12 on heating rates is negligible, so most studies focus on the forcing by these molecules at the surface. We use methods 2 and 3 to deal with the overlap of CFC11 and CFC12 with other gases. For a CFC11 concentration of 280 parts per trillion by volume (pptv), forcing at the surface is 0.076 W m^{-2} for MLS, 0.056 W m^{-2} for TRO, and 0.075 W m^{-2} for SAW. For CFC12 at 530 pptv, corresponding forcings at the surface are 0.19, 0.14, and 0.18 W m^{-2} . This is consistent with other studies (e.g., Christidis et al. 1997).

TABLE 9. Comparisons of absorbed solar energy inside the atmosphere, downward flux at surface, and upward flux at the TOA in range of 0–50 000 cm^{-1} with $\text{O}_3 + \text{CO}_2 + \text{H}_2\text{O} + \text{O}_2$. Incoming solar flux, CO_2 , and surface albedo are set as 1357.96 W m^{-2} , 346 ppv, and 0. For each item, the first column shows results of GFDL line-by-line plus doubling-adding calculations [Table 7 of Freidenreich and Ramaswamy (1999)], the second column shows model results, and the relative differences in percentage (%) are shown in parentheses.

Profile	θ_0	Absorbed			Downward			Upward		
		(W m^{-2})	Percent		(W m^{-2})	Percent		(W m^{-2})	Percent	
TRO	0	249.1	248.4	(-0.2)	1058.8	1060.2	(0.1)	50.1	49.4	(-1.4)
TRO	53	172.9	171.8	(-0.6)	596.2	600.2	(0.7)	45.7	45.3	(-0.9)
TRO	75	94.0	92.2	(-1.9)	221.7	223.7	(0.9)	35.8	35.5	(-0.8)
MLS	0	233.7	232.8	(-0.4)	1074.8	1076.3	(0.1)	49.5	48.9	(-1.2)
MLS	53	163.7	161.9	(-1.1)	606.1	610.5	(0.7)	45.1	44.9	(-0.4)
MLS	75	90.5	88.5	(-2.2)	225.6	227.8	(1.0)	35.4	35.1	(-0.9)
SAW	0	156.7	158.0	(0.8)	1152.8	1152.0	(-0.1)	48.5	48.0	(-1.0)
SAW	53	114.1	114.2	(0.1)	656.6	659.1	(0.4)	44.1	43.9	(-0.5)
SAW	75	68.0	67.2	(1.1)	249.1	249.9	(0.3)	34.1	34.3	(-0.6)

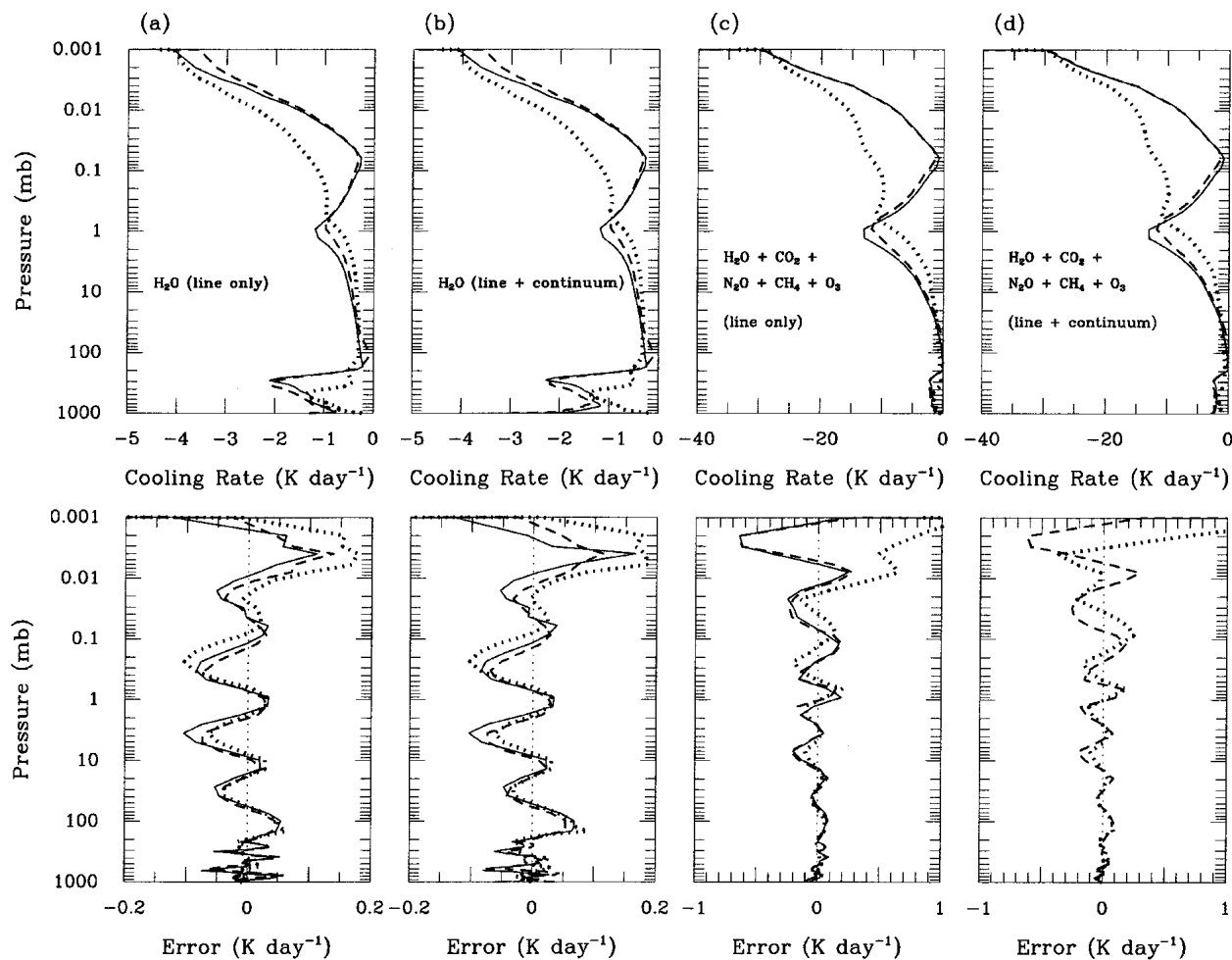


FIG. 12. (a), (b) Heating rate profiles and corresponding errors for H_2O lines only and lines plus continuum in $0\text{--}540 + 800\text{--}2500\text{ cm}^{-1}$. (c), (d) Heating rate profiles and corresponding errors for $\text{H}_2\text{O} + \text{CO}_2 + \text{N}_2\text{O} + \text{CH}_4 + \text{O}_3$ lines only and lines plus continuum in $0\text{--}2500\text{ cm}^{-1}$. Solid, dashed, and dotted lines as in Fig. 3. The mixing ratio of CO_2 is 350 ppm.

4. Radiative transfer above the stratosphere and strategies for efficiency

For some intervals in CPS the corresponding gaseous absorption coefficients are very large. This characteris-

tic can be used to dramatically simplify the radiative transfer process. For solar radiation, g_i are divided into two groups. Group 1 contains g_i located very close 1 in CPS with very large absorption coefficients, and consequently large optical depths in the upper atmosphere.

TABLE 10. Comparisons of upward flux (W m^{-2}) for the infrared $0\text{--}2500\text{ cm}^{-1}$ at the TOA and downward flux (W m^{-2}) at the surface for three atmospheric profiles. The numbers on the left are line-by-line results; the numbers on the right are model results. Differences are shown in the parentheses (W m^{-2}); water only in spectra $0\text{--}540$ and $800\text{--}2500\text{ cm}^{-1}$ and $\text{H}_2\text{O} + \text{CO}_2 + \text{O}_3 + \text{N}_2\text{O}$ in $0\text{--}2500\text{ cm}^{-1}$, with absorption line only and line + continuum.

	H_2O 0–540 and 800–2500 cm^{-1} (line)		H_2O 0–540 and 800–2500 cm^{-1} (line + continuum)		$\text{H}_2\text{O}+\text{CO}_2+\text{O}_3+\text{N}_2\text{O}$ 0–2500 cm^{-1} (line)		$\text{H}_2\text{O}+\text{CO}_2+\text{O}_3+\text{N}_2\text{O}$ 0–2500 cm^{-1} (line + continuum)	
	$F^+(\text{TOA})$							
MLS	236.14	235.80 (−0.34)	229.92	229.62 (−0.30)	290.70	290.48 (−0.22)	283.58	283.18 (−0.40)
TRO	249.23	248.91 (−0.32)	239.30	238.89 (−0.41)	303.85	303.66 (−0.19)	292.89	292.37 (−0.52)
SAW	157.21	156.77 (−0.43)	155.63	155.18 (−0.45)	201.49	200.80 (−0.69)	199.89	199.08 (−0.81)
	$F^-(\text{surface})$							
MLS	199.99	199.81 (−0.18)	232.43	232.51 (0.08)	306.02	304.92 (−1.10)	344.59	344.37 (−0.22)
TRO	221.24	220.96 (−0.30)	270.13	269.89 (−0.24)	334.88	334.33 (−0.53)	390.77	390.24 (−0.53)
SAW	105.89	106.23 (0.34)	112.12	112.61 (0.49)	164.64	164.82 (0.16)	172.94	173.11 (0.17)

In this group g_i are called minor intervals. For a minor interval, incoming solar flux is attenuated quickly as it travels down through the atmosphere. Intervals in group 1 were selected carefully so that the incoming solar flux (for overhead sun) is attenuated to less than 0.1 W m^{-2} at the surface for all three standard atmospheric profiles. For such intervals, there is no underlying surface reflection and no reflection from the lower atmosphere since Rayleigh scattering is negligible for two reasons. First, Rayleigh optical depth is much smaller than the gaseous optical depth in these intervals. Second, Rayleigh scattering is proportional to air density, which is small in the upper atmosphere.

Without scattering and reflection, downward flux can be simply obtained. Assume that level 1 is the TOA, level N is the surface, and layer j is between levels j and $j + 1$. For the i th g_i , flux at level $j + 1$ is

$$F_{j+1}^i = \exp(-\cos\theta_0 \langle k \rangle_j^i q \Delta p / G) F_j^i, \quad (15)$$

where θ_0 is solar zenith angle, $\langle k \rangle_j^i$ is absorption coefficient for interval g_i at layer j , q is the scaled absorber amount, and Δp is pressure thickness for layer j . The boundary condition at the TOA is $F_1^i = \cos\theta_0 S_i$, where S_i is the solar incoming flux for interval g_i . This greatly simplifies the computation of flux transmission (see Gabriel et al. 2001).

The remaining g_i are classified into group 2. They have much smaller absorption coefficients compared to those in group 1. The g_i in this group are referred to as major intervals. Contributions to heating by this group are mostly below the 1-mb height, and the full radiative transfer process is required. However, since solar heating is negligible above 1 mb for this major group, we need only consider radiative transfer between 1 mb and the surface. Above 1 mb, downward flux is $\cos\theta_0 S_i$ and upward flux equals that at 1 mb.

Likewise for the infrared, g_i are divided into two groups. Group 1 contains g_i with large absorption coefficients that cool the upper atmosphere. However, calculation of flux above 1 mb for the infrared cannot be neglected since the flux is produced mostly from local thermal emission. But since optical depths are very large and transmittance very small, radiative transfer can be simplified by neglecting aerosol and even cloud optical depth in such intervals.

For group 2 with smaller absorption coefficients, full radiative transfer is required. As in the solar, radiative transfer need only be performed between 1 mb and the surface. Table 1 lists the numbers for the major interval, the minor interval, and the minor interval only applied above 1 mb.

5. Spectrum overlap of the solar and infrared

Traditionally in climate models, the solar spectrum is from 2500 to $50\,000 \text{ cm}^{-1}$, and the infrared from 0 to 2500 cm^{-1} . However in $0\text{--}2500 \text{ cm}^{-1}$ there is about 12

W m^{-2} incoming solar flux at the TOA. If not treated as direct solar radiation, this incoming solar energy should be imposed onto the downward flux for the appropriate infrared bands. Table 1 lists incoming solar energies for each infrared band. Usually, infrared downward flux can be written as

$$F^-(p) = \pi \int_0^p B(T') \frac{\partial \Psi[\kappa(p, p')]}{\partial p'} dp', \quad (16)$$

where $F^-(p)$ is downward flux at pressure p , T' is temperature at pressure p' , and $\Psi[\kappa(p, p')]$ is flux transmittance defined in terms of the absorptance depth $\kappa(p, p')$ for a slab of atmosphere between p and p' . With solar energy input into the infrared range it can be proven that the solution is the same as (16) but with an additional term: $\mu_0 \pi S_0 e^{-\tau(p, 0)/\mu_0}$, where πS_0 is the incoming solar flux at the TOA, and $\tau(p, 0)$ is the optical depth from the TOA to the pressure level p .

There is another kind of solution in which all exchange contributions from outside a layer are represented by incoming flux at the boundary of the layer (Fu et al. 1997; Li 2002). For this kind of solution, it can be proven that the upper boundary condition for downward flux at the TOA should be changed from $F_1^- = 0$ to $F_1^- = \mu_0 \tilde{S}_0$.

Figure 13 shows the change in cooling rate for $0\text{--}2500 \text{ cm}^{-1}$ when incoming solar energy in $0\text{--}2500 \text{ cm}^{-1}$ is included. The top panels show cooling rates for three θ_0 and three atmospheric profiles. The bottom panels are corresponding differences in the cooling rate with and without solar energy. It is shown that the cooling rate profiles are affected by treating the overlap of the solar and infrared spectra. The large solar heating rate is due mostly to the $4.3\text{-}\mu\text{m}$ CO_2 band in $2200\text{--}2500 \text{ cm}^{-1}$. Part of the heating rate by the $4.3\text{-}\mu\text{m}$ CO_2 band has been discussed in section 2. However, as we mentioned before, this heating rate would not be true because of the non-LTE effect.

It is found that the interaction of solar and infrared radiation is weak in the $0\text{--}2500 \text{ W m}^{-2}$ range. This means that the result obtained by adding the individual calculations from solar and thermal infrared is close to the result obtained when solar and thermal infrared are calculated together as shown above. One advantage for considering the solar and infrared interactions together is that many fewer radiative transfer processes are required. The disadvantage is that the solar flux cannot be treated explicitly and so surface reflection of solar flux cannot be considered. Fortunately, the downward solar flux at the surface in $0\text{--}2500 \text{ cm}^{-1}$ is very small even for clear sky. The maximum is about 2 W m^{-2} for the unrealistic situation of SAW at overhead sun.

6. Conclusions

A new radiation scheme based on the CKD method for gaseous transmission was proposed. First, however,

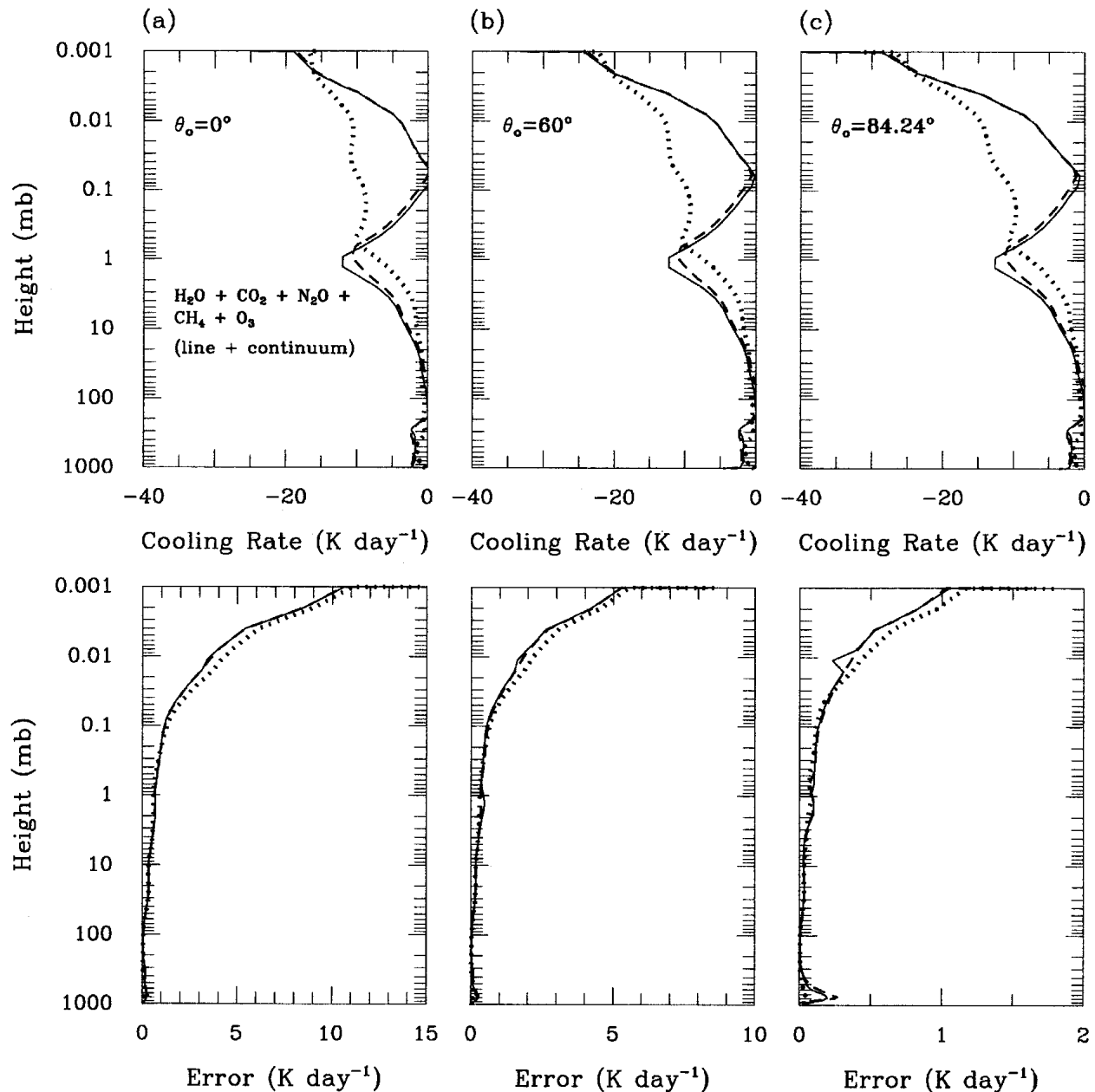


FIG. 13. (top) Heating rate profiles for $\text{H}_2\text{O} + \text{CO}_2 + \text{N}_2\text{O} + \text{CH}_4 + \text{O}_3$ lines plus continuum in $0\text{--}2500\text{ cm}^{-1}$ for three solar zenith angles when incoming solar radiation is treated as thermal radiation. (bottom) Differences in heating with and without incoming solar energy. Solid, dashed, and dotted lines as in Fig. 3. The mixing ratio of CO_2 is 350 ppm.

the mathematical foundation for the k distribution was reconsidered. It was found that each interval in CPS contributes mostly to heating rate (and its error) at fairly localized altitudes. Therefore, a strategy was proposed to determine the widths of the intervals in CPS: for a particular interval, minimize the heating rate errors at altitudes where heating rates are maximal for the interval in question.

Much of this paper was devoted to the discussion of the overlap of two or more gases. Three schemes for

gaseous overlap were discussed. Method 1 sorts the appropriate combination of the two gaseous absorption coefficients as though it were one gas. This method applies to cases in which two gases interact very strongly. Generally, correct results are obtained when both gases are present, but not for each gas on its own. Method 2 is the most general method because it addresses gases that contribute mostly to heating at different altitudes by portioning the roles of gases into different intervals in CPS. Hence, in each interval a

certain gas is designated as the major gas and its absorption coefficient is sorted in that interval. Thus, the relative importance of each gas can be explicitly addressed. Method 3 is applied to the minor gases associated with small heating rates. This method adjusts absorption coefficients only slightly for the first few intervals of CPS to make the radiative forcing of the minor gas match line-by-line calculations.

The computational efficiency of a radiation algorithm is a key factor if it is to be used in a climate model. First, it is proposed that as few as possible intervals in CPS be used, but that errors in heating rates be limited to allowed ranges. Second, characteristics of those intervals with very large absorption coefficients are exploited, thereby simplifying the calculation process. This is especially effective for solar radiation where the complicated radiative transfer process can be reduced simply to Beer's law of transmission (cf. Gabriel et al. 2001). Third, continuum treatment is simplified by neglecting its effect in some unimportant intervals and at high altitudes. Fourth, for gaseous overlap, the very simple and efficient methods 2 and 3 are widely applied. Fifth, by keeping the total number of intervals in CPS small, much of the energy is concentrated in only a few intervals. This is beneficial for noise reduction in the Monte Carlo independent column approximation (McICA) method (Barker et al. 2002; Räisänen and Barker 2004) and Monte Carlo simulations of broadband radiative transfer. All in all, this CKD model is very efficient, yet accurate, for it executes roughly 10 times faster than most existing CKD models.

Acknowledgments. The authors would like to thank Drs. M.-D. Chou and E. Mlawer for a lot of help in the line-by-line calculation and continuum evaluation, and for helpful discussion. The authors also would like to thank Drs. V. Fomichev, P. Räisänen, Z. Sun, and R. West for their helpful comments. This work was partly supported through funding of the Modeling of Clouds and Climate Proposal by the Canadian Foundation for Climate and Atmospheric Sciences, the Meteorological Service of Canada, and the Natural Sciences and Engineering Research Council. Also, HB was supported by Grant DE-FG02-90ER61071 from the U.S. Department of Energy's Atmospheric Radiation Measurement (ARM) Program.

APPENDIX A

k-Distribution Function

It can be shown (e.g., Galindo and Pascual 1989) that if a function $h(x)$ has n zeros at x_1, x_2, \dots, x_n , then

$$\delta[h(x)] = \sum_{i=1}^n \frac{1}{h'(x_i)} \delta(x - x_i), \quad (\text{A1})$$

where $h'(x)$ is the derivative of $h(x)$ with respect to x . The k -distribution function,

$$f(k) = \frac{1}{\Delta\nu} \int_{\Delta\nu} \delta[k - k(\nu)] d\nu, \quad (\text{A2})$$

can be rewritten in a form similar to (A1) as

$$f(k) = \frac{1}{\Delta\nu} \int_{\Delta\nu} \sum_{i=1}^n \delta[k - k(\nu_i)] d\nu, \quad (\text{A3})$$

in which ν_i are frequencies corresponding to the zeros of $k - k(\nu)$ within the range $\Delta\nu$. The δ functions in (A3) pick out and gather together all points of $k(\nu)$ that equal k . Usually in physics the summation of δ functions in (A1) or (A3) is called a Dirac comb.

Equation (A1) can also be written in discrete form. Since the derivative of the step function H equals the δ function,

$$f(k) = \frac{1}{\Delta\nu} \int_{\Delta\nu} \sum_{i=1}^n \lim_{\delta\nu_i \rightarrow 0} \frac{H[k - k(\nu_i + \delta\nu_i)] - H[k - k(\nu_i - \delta\nu_i)]}{k(\nu_i + \delta\nu_i) - k(\nu_i - \delta\nu_i)} d\nu, \quad (\text{A4})$$

where $\delta\nu_i$ is a limited interval around ν_i . Further from (A4),

$$\begin{aligned} f(k) &\approx \frac{1}{\Delta\nu} \int_{\Delta\nu} \sum_{i=1}^n \frac{|H[k - k(\nu_i + \delta\nu_i)] - H[k - k(\nu_i - \delta\nu_i)]|}{2 \left| \frac{dk_\nu}{d\nu} \right|_i \delta\nu_i} d\nu \\ &= \frac{1}{\Delta\nu} \sum_{i=1}^n |H[k - k(\nu_i + \delta\nu_i)] - H[k - k(\nu_i - \delta\nu_i)]| \left| \frac{d\nu}{dk_\nu} \right|_i, \end{aligned} \quad (\text{A5})$$

in which the two step functions form a window function around ν_i and the integral over ν is zero outside the window. Equation (A5) is only an approximation that produces the mean value of $k(\nu)$ within each window function. In (A3), however, the exact value of $k(\nu_i)$ at ν_i is selected. Based on (A5), the space transform of (4) cannot be achieved. Equation (A5) is shown also by Goody and Yung (1989).

APPENDIX B

Inequality Relation

For m positive numbers a_1, a_2, \dots, a_m , the arithmetic-geometric inequality (e.g., Gradshteyn and Ryzhik 1980) states that

$$\left(\frac{\sum_{i=1}^m a_i}{m} \right)^m \geq \prod_{i=1}^m a_i, \quad (\text{B1})$$

where the equality holds only for $a_1 = a_2 = \dots = a_m$. Equation (B1) can then be used to prove the integral inequality relation

$$\int_{G_{i-1}}^{G_i} e^{-wk(g')} dg' \geq \exp \left[-w \frac{1}{g_i} \int_{G_{i-1}}^{G_i} k(g') dg' \right] g_i, \quad (\text{B2})$$

in which the equality exists for constant $k(g')$.

Begin by rewriting the left-hand side of (B2) as

$$\int_{G_{i-1}}^{G_i} e^{-wk(g')} dg' = \lim_{m \rightarrow \infty} \sum_{j=1}^m e^{-wk_j} \delta g', \quad (\text{B3})$$

where $\delta g' = (G_i - G_{i-1})/m = g_i/m$. Then, following from (B1) we have for the right-hand portion of (B3),

$$\left(\frac{\delta g'}{g_i} \sum_{i=1}^m e^{-wk_i} \right)^{g_i/\delta g'} \geq e^{-w \sum_{i=1}^m k_i}, \quad (\text{B4})$$

and thus,

$$\sum_{j=1}^m e^{-wk_j} \delta g' \geq \exp \left[-w \frac{1}{g_i} \sum_{j=1}^m k_j \delta g' \right] g_i. \quad (\text{B5})$$

In the limit as $m \rightarrow \infty$, (B2) and (B5) are equivalent. The inequality shown in the text as (9) is based on (B2). This kind of inequality relation is also true in frequency space. Assuming that

$$\text{Tr}(w) = \sum_{i=1}^N \int_{\nu_{i-1}}^{\nu_i} e^{-wk(\nu)} d\nu = \sum_{i=1}^N e^{-w\langle k_i \rangle} \Delta \nu_i, \quad (\text{B6})$$

where $\Delta \nu_i = \nu_i - \nu_{i-1}$ and N is the number of bands,

$$\langle k_i \rangle = \frac{\alpha_i}{\Delta \nu_i} \int_{\nu_{i-1}}^{\nu_i} k(\nu) d\nu, \quad (\text{B7})$$

where $\alpha_i \leq 1$. The equality being true for constant $k(\nu)$ within the interval $\Delta \nu_i$.

REFERENCES

- Barker, H. W., R. Pincus, and J.-J. Morcrette, 2002: The Monte Carlo Independent Column Approximation: Application within large-scale models. *Proc. Workshop on the Representation of Cloud Systems in Large-Scale Models*, Kananaskis, AB, Canada, GCSS-ARM, 20–24.
- Chou, M.-D., and M. J. Suarez, 1999: A solar radiation parameterization for atmospheric studies. NASA Tech. Memo. 104606, 40 pp.
- , —, X.-Z. Liang, and M.-H. Yan, 2001: A thermal infrared radiation parameterization for atmospheric studies. NASA Tech. Memo. 104609, 56 pp.
- Christidis, N., M. D. Hurley, S. Pinnock, K. P. Shine, and T. J. Wallington, 1997: Radiative forcing of climate change by CFC-11 and possible CFC replacements. *J. Geophys. Res.*, **102**, 19 597–19 609.
- Edwards, J. M., and A. Slingo, 1996: Studies with a flexible new shortwave radiation code. I: Choosing a configuration for a large-scale model. *Quart. J. Roy. Meteor. Soc.*, **122**, 689–719.
- Freidenreich, S., and V. Ramaswamy, 1999: A new multiple-band solar radiative parameterization for general circulation models. *J. Geophys. Res.*, **104**, 31 389–31 409.
- Fu, Q., and K. N. Liou, 1992: On the correlated k -distribution method for radiative transfer in nonhomogeneous atmospheres. *J. Atmos. Sci.*, **49**, 2139–2156.
- , —, M. C. Cribb, T. P. Charlock, and A. Grossman, 1997: On multiple scattering in thermal infrared radiative transfer. *J. Atmos. Sci.*, **54**, 2799–2812.
- Gabriel, P. M., P. T. Partain, and G. L. Stephens, 2001: Parameterization of atmospheric radiative transfer. Part II: Selection rules. *J. Atmos. Sci.*, **58**, 3411–3423.
- Galindo, A., and P. Pascual, 1989: *Quantum Mechanics I*. Springer-Verlag, 417 pp.
- Goody, R. M., and Y. L. Yung, 1989: *Atmospheric Radiation: Theoretical Basis*. Oxford University Press, 519 pp.
- , R. West, L. Chen, and D. Crisp, 1989: The correlated k method for radiation calculations in nonhomogeneous atmospheres. *J. Quant. Spectrosc. Radiat. Transfer*, **42**, 539–550.
- Gradshteyn, I. S., and I. M. Ryzhik, 1980: *Table of Integrals, Series, and Products*. Academic Press, 1160 pp.
- Holling, H.-D., 1993: A k -distribution method considering centers and wings of atmospheric absorption lines. *J. Geophys. Res.*, **98**, 2747–2756.
- Kato, S., T. P. Ackerman, J. H. Mather, and E. E. Clothiaux, 1999: The k -distribution method and correlated k -approximation for a shortwave radiative transfer model. *J. Quant. Spectrosc. Radiat. Transfer*, **62**, 109–121.
- Kratz, D. P., 1995: The correlated k -distribution technique as applied to the AVHRR channels. *J. Quant. Spectrosc. Radiat. Transfer*, **53**, 501–517.
- Lacis, A. A., and V. Oinas, 1991: A description of the correlated k -distribution method modeling non-grey gaseous absorption, thermal emission, and multiple scattering in vertical inhomogeneous atmosphere. *J. Geophys. Res.*, **96**, 9027–9063.
- Li, J., 2002: Accounting for unresolved clouds in a 1D infrared radiative transfer model. Part I: Solution for radiative transfer, cloud scattering, and overlap. *J. Atmos. Sci.*, **59**, 3302–3320.
- McClatchey, R. A., R. W. Fenn, J. E. A. Selby, F. E. Volz, and J. S. Garing, 1972: Optical properties of the atmosphere. 3d ed. AFCRL-72-0497, 108 pp.
- Mlawer, E. J., S. J. Taubman, P. D. Brown, M. J. Iacono, and S. A. Clough, 1997: Radiative transfer for inhomogeneous atmosphere: RRTM, a validated correlated- k model for the longwave. *J. Geophys. Res.*, **102**, 16 663–16 682.
- Räisänen, P., and H. Barker, 2004: Evaluation and optimization of sampling errors for Monte Carlo independent column approximation. *Quart. J. Roy. Meteor. Soc.*, **130**, 2047–2068.
- Ramaswamy, V., and S. M. Freidenreich, 1991: Solar radiative line-by-line determination of water vapor absorption and water cloud extinction in inhomogeneous atmospheres. *J. Geophys. Res.*, **96**, 9133–9157.
- Strobel, M. R., 1978: Parameterization of the atmospheric heating rate from 15 to 120 km due to O_2 and O_3 absorption of solar radiation. *J. Geophys. Res.*, **83**, 6225–6230.
- Sun, Z., and L. Rikus, 1999: Improved application of ESFT to inhomogeneous atmosphere. *J. Geophys. Res.*, **104**, 6291–6303.
- West, R., D. Crisp, and L. Chen, 1990: Mapping transformations for broadband atmospheric radiation calculations. *J. Quant. Spectrosc. Radiat. Transfer*, **43**, 191–199.
- Yang, S., P. Ricchiazzi, and C. Cautier, 2000: Modified correlated k -distribution method for remote sensing. *J. Quant. Spectrosc. Radiat. Transfer*, **64**, 585–608.
- Zhang, H., T. Nakajima, G. Shi, T. Suzuki, and R. Imasu, 2003: An optional approach to overlapping bands with correlated k distribution method and its application to radiative transfer calculations. *J. Geophys. Res.*, **108**, 4641, doi:10.1029/2002JD003358.